Burns & Trauma, 2026, 14, tkag063
https://doi.org/10.1093/burnst/tkag063
Published: 18 September 2026
Research Article

OXFORD

RUNX1 links ATF4-associated stress adaptation to microenvironmental remodeling in POSTN+ fibroblasts during skin fibrosis

Binyu Song[‡], Yuhan Zhu[‡], Xiang Wang[‡], Yige Han[‡], Junying Song, Kai Wang, Tong Wang, Yixuan Peng, Xiaozi Liu, Zhiwei Cui, Peng Guo, Yajuan Song, Yi Shi, Zhou Yu[*], Baoqiang Song[*]

Department of Plastic Surgery, Xijing Hospital, Fourth Military Medical University, No. 127 Changle West Road, Xincheng District, Xi'an 710032, Shaanxi Province, People's Republic of China

[*]Corresponding authors. Zhou Yu, E-mail: yz20080512@163.com; Baoqiang Song, E-mail: songbq@fmmu.edu.cn
[‡]Binyu Song, Yuhan Zhu, Xiang Wang, and Yige Han contributed equally.

Abstract

Background: **Skin fibrosis encompasses a spectrum of disorders and includes hypertrophic scar (HTS), keloid scar (KS), and systemic sclerosis (SSc), but the pathogenic fibroblast states and shared upstream regulators contributing to these conditions remain incompletely defined. As a common form of skin fibrosis, HTS provides a useful model for elucidating fibroblast heterogeneity and mechanism-based therapeutic vulnerability across skin fibrosis diseases. This study aimed to define the role of RUNX1 in pathogenic POSTN+ fibroblasts during skin fibrosis and to investigate the underlying stress-adaptive and microenvironment-remodeling mechanisms.**

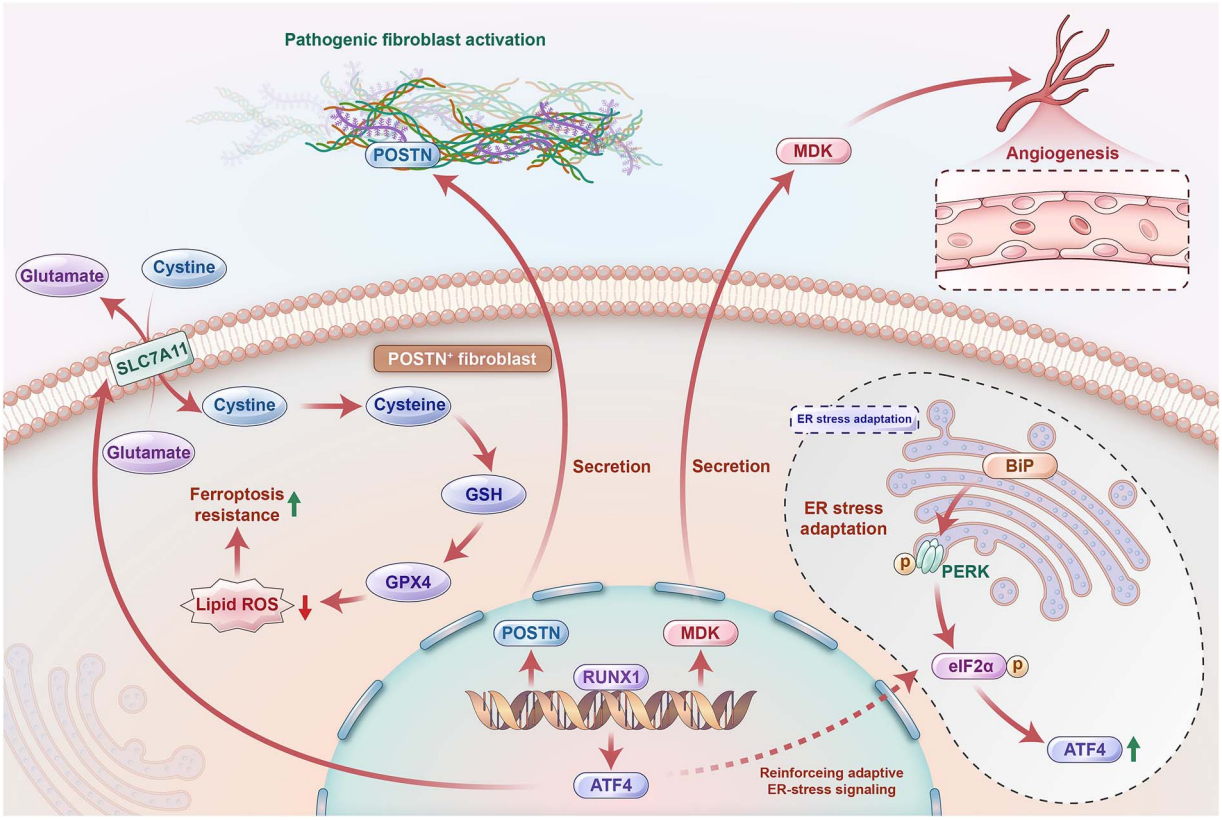
Methods: **We performed single-cell RNA sequencing, spatial transcriptomic analysis, multiomics profiling, and cell–cell communication analysis to identify pathogenic fibroblast subpopulations and their regulatory networks in HTS. RUNX1-centered mechanisms were analyzed by CUT&Tag, RNA sequencing, rescue experiments, and functional assays, followed by *in vitro* and *in vivo* validation. High-throughput virtual screening and structural analyses were used to computationally prioritize candidate compounds predicted to bind to POSTN that are relevant to the RUNX1-high POSTN+ fibroblast state.**

Results: **The integrated analyses revealed a significantly expanded RUNX1-high POSTN+ fibroblast subpopulation in HTS and KS. RUNX1 expression was consistently elevated across human skin fibrosis diseases and experimental models of skin fibrosis. Mechanistically, RUNX1 increased the pathogenic properties of POSTN+ fibroblasts by activating ATF4 and POSTN. Through ATF4, RUNX1 increased endoplasmic reticulum stress adaptation and ferroptosis resistance, thereby supporting the ability of POSTN+ fibroblasts to remain activated under stress. Through POSTN, RUNX1 further reinforced fibroblast activation and matrix remodeling. Furthermore, RUNX1 transcriptionally activated MDK, which promoted angiogenesis-associated microenvironmental remodeling through paracrine signaling. Our computational analysis prioritized berberine (BBR) as a candidate compound predicted to bind to POSTN and BBR suppressed RUNX1/POSTN-associated stress-adaptive and profibrotic features in hypertrophic scar fibroblasts. *In vivo* validation using a bleomycin-induced skin fibrosis mouse model and a mouse scar model supported the antifibrotic potential of targeting RUNX1, and BBR reduced scar formation in a rabbit ear hypertrophic scar model, demonstrating its antiscar therapeutic efficacy.**

Conclusion: **RUNX1 serves as a universal marker and actionable upstream regulator in skin fibrosis diseases. RUNX1-high POSTN+ fibroblasts may contribute to skin fibrosis by increasing the adaptation to ATF4-associated endoplasmic reticulum stress, ferroptosis resistance, persistent fibroblast activation, and vascular microenvironmental remodeling. BBR therefore represents a potential candidate predicted to bind to POSTN for skin fibrosis treatment.**

Received: 8 May 2026. **Revised:** 15 September 2026. **Accepted:** 16 September 2026
© The Author(s) 2026. Published by Oxford University Press.
This is an Open Access article distributed under the terms of the Creative Commons Attribution-NonCommercial License (https://creativecommons.org/licenses/by-nc/4.0/), which permits non-commercial re-use, distribution, and reproduction in any medium, provided the original work is properly cited. For commercial re-use, please contact reprints@oup.com for reprints and translation rights for reprints. All other permissions can be obtained through our RightsLink service via the Permissions link on the article page on our site—for further information please contact journals.permissions@oup.com.

Graphical abstract



Keywords POSTN+ fibroblasts, RUNX1, Skin fibrosis, Ferroptosis, Endoplasmic reticulum stress, Microenvironmental remodeling

Highlights

- **RUNX1 expression is broadly increased across different human and animal skin fibrosis tissues and promotes myofibroblast activation.**
- **RUNX1 activates ATF4 to sustain POSTN+ fibroblasts via the PERK-ATF4/SLC7A11-GPX4 axes.**
- **RUNX1 transcriptionally activates POSTN and MDK to sustain fibroblast activation and angiogenesis.**
- **Berberine is a candidate compound predicted to bind to POSTN that attenuates fibroblast activation and profibrotic stress-adaptive features.**

Background

Skin fibrosis comprises a spectrum of cutaneous disorders and includes hypertrophic scar (HTS), keloid scar (KS), and systemic sclerosis (SSc) [1]. Although these conditions occur in distinct clinical contexts and differ in etiology, anatomical distribution, and disease course, they share core pathological features characterized by persistent fibroblast activation, excessive extracellular matrix (ECM) deposition, and progressive dermal remodeling [1–4]. This pathological convergence suggests that common cellular and molecular mechanisms may underlie diverse skin fibrosis diseases [3]. Fibroblasts play a central role in cutaneous fibrogenesis [4, 5], yet the shared pathogenic fibroblast states that drive disease progression across the spectrum of skin fibrosis diseases remain incompletely understood [6]. Among these disorders, HTS is among the most prevalent and clinically accessible forms of skin fibrosis, making them a useful model for identifying shared fibroblast-dependent mechanisms and therapeutic targets with broader relevance across skin fibrosis diseases.

Recent single-cell studies have upended the traditional view of fibroblasts as a uniform mesenchymal population, instead revealing widespread fibroblast heterogeneity in fibrotic tissues [6, 7]. Single-cell RNA sequencing revealed four fibroblast subpopulations in keloid, including expanded mesenchymal fibroblasts, suggesting that cutaneous fibrosis may be driven by pathogenic fibroblast states rather than uniform fibroblast activation [6]. Among activated fibrogenic fibroblasts, periostin-expressing (POSTN+) fibroblasts are of particular interest. Shared POSTN+ activated fibroblast subsets have been recognized across organs [8], and in the context of pulmonary fibrosis, ablation of POSTN+ myofibroblasts after injury markedly ameliorates fibrosis [9]. In skin disease, POSTN+ fibroblasts have likewise been linked to

pathogenic cell–cell communication [10]. These findings suggest that POSTN+ fibroblasts may represent a conserved pathogenic fibroblast state in skin fibrosis. However, whether and how this state contributes to cutaneous fibrotic progression and which upstream factors help maintain its pathogenic activity remain to be determined.

RUNX1 is best known for its roles in lineage specification and developmental regulation, but increasing evidence has revealed its role in fibrotic remodeling in multiple organs [11–13]. In pulmonary fibrosis, TGF-β induces RUNX1 expression during fibroblast activation, while RUNX1 inhibition blocks lung fibroblast-to-myofibroblast differentiation [11]. RUNX1 has also been implicated in renal fibrosis and promotes liver fibrosis through TGF-β/Smad signaling [14, 15]. In skin disease, RUNX1 has been detected in a subset of dermal fibroblasts and associated with disease severity in systemic sclerosis [16]. Notably, recent cardiac studies connected RUNX1 to POSTN-associated fibrotic fibroblast states by showing that RUNX1 regulates POSTN expression and that RUNX1 in POSTN-expressing fibroblasts exacerbates adverse remodeling after myocardial infarction [17]. However, compared with that in other organ fibrosis models, the role of RUNX1 in the spectrum of skin fibrosis diseases, particularly in HTS-, KS-, and SSc-associated POSTN+ fibroblast states, remains insufficiently defined. Therefore, the present study sought to determine whether RUNX1 acts as a cell state-associated upstream regulator of POSTN+ fibroblasts in skin fibrosis rather than merely as a general marker of fibroblast activation.

Fibrotic skin is not a passive structural lesion but a hostile niche characterized by abnormal mechanical tension, sustained extracellular matrix biosynthetic demand, oxidative stress, and proteostatic burden. Under such conditions, pathogenic fibroblasts likely require stress-adaptive mechanisms to remain persistently activated and fibrogenic [18–20]. Endoplasmic reticulum (ER) stress and its associated adaptive pathways, particularly the PERK–eIF2α–ATF4 axis, constitute important mechanisms through which cells manage such stress through the reprogramming of protein translation, amino acid metabolism, and antioxidant defenses [19, 21]. Moreover, ferroptosis, an iron-dependent form of regulated cell death driven by excessive lipid peroxidation, has been increasingly implicated in fibrotic pathology, including skin fibrosis, with redox-buffering systems such as the SLC7A11/GPX4 axis serving as major determinants of ferroptosis susceptibility [22–24]. In skin fibrosis, systemic sclerosis fibroblasts exhibit GPX4-driven ferroptosis resistance, whereas recent studies on pathological scarring suggest that promoting fibroblast or myofibroblast ferroptosis can attenuate hypertrophic scar formation and may also contribute to antikeloid efficacy [4, 25]. ATF4 is a central regulator of amino acid metabolism and redox homeostasis and plays a key role in connecting ER stress adaptation with resistance to ferroptotic damage [21, 26, 27]. Together, these findings suggest that adaptation to proteostatic and oxidative stress may be a key feature enabling fibrotic fibroblasts to persist under hostile conditions. However, whether POSTN+ fibroblast states in skin fibrosis are linked to ER stress adaptation and ferroptosis-related survival pathways and whether RUNX1 coordinates this process remain unclear. We therefore speculated that RUNX1 may sustain pathogenic POSTN+ fibroblasts by coordinating ER stress adaptation and ferroptosis resistance, thereby promoting their continued survival, activation, and pathogenesis in skin fibrosis.

Fibroblasts are increasingly recognized not only as extracellular matrix-producing effector cells but also as active organizers of the fibrotic niche [1, 28]. This is particularly relevant in skin fibrosis, where lesions exhibit not only excessive collagen deposition but also vascular abnormalities and a dysregulated repair microenvironment [1, 29]. These features suggest that pathogenic fibroblast states may influence tissue remodeling through paracrine signaling and intercellular crosstalk [1, 28]. Consistent with these findings, fibroblast-derived signals can directly increase endothelial proliferation, migration, and tubulogenesis [30], and in skin disease, POSTN+ fibroblasts have been linked to pathogenic communication with SPP1+ myeloid cells [10]. These findings raise the possibility that pathogenic POSTN+ fibroblasts contribute to skin fibrosis progression not only through matrix production but also through vascular dysregulation and local microenvironmental remodeling. Whether RUNX1 connects this POSTN+ fibroblast state to endothelial-associated microenvironmental remodeling remains unclear. We therefore speculated that RUNX1 may promote skin fibrosis by driving a POSTN+ fibroblast state with increased niche-remodeling capacity, thereby contributing to vascular dysregulation and local microenvironmental remodeling.

To investigate the role of RUNX1 in skin fibrosis and explore a mechanism-based therapeutic strategy directed toward the RUNX1-high POSTN+ fibroblast state, we performed integrated multiomics analyses together with *in vitro* and *in vivo* validation. Our results demonstrate that RUNX1 is consistently upregulated in human skin fibrosis diseases, including HTS, KS, and SSc, as well as in multiple experimental models of skin fibrosis and scarring, underscoring its role as a common marker and actionable upstream regulator of skin fibrosis. We further show that RUNX1 sustains a pathogenic POSTN+ fibroblast state by promoting ATF4-associated ER stress adaptation, ferroptosis resistance, persistent fibroblast activation, and vascular microenvironmental remodeling. Moreover, through high-throughput screening followed by experimental validation, we identified berberine (BBR) as a candidate small molecule predicted to bind to POSTN that is associated with RUNX1-high POSTN+ fibroblasts. Taken together, these findings define a RUNX1-high POSTN+ fibroblast state in skin fibrosis and reveal its stress-adaptive, ferroptosis resistance, and niche remodeling mechanisms, thereby highlighting the translational potential of the RUNX1-high POSTN+ fibroblast state as a candidate therapeutic vulnerability.

Methods

Clinical sample collection and single-cell RNA-seq data sources

Human skin samples were obtained from the Department of Plastic Surgery, Xijing Hospital. This study was approved by the Ethics Committee of Xijing Hospital, Air Force Medical University (KY20242186–C-1), and all procedures involving human tissue sampling and processing were conducted in accordance with the Declaration of Helsinki. Written informed consent was obtained from all participants before sample collection. A total of 22 human skin samples, comprising 10 HTS samples, 6 KS samples, and 6 normal skin (NS) samples, were included in this study. Among these, three HTS tissues were used for single-cell RNA sequencing, whereas the remaining samples were subjected to immunohistochemistry (IHC), western blotting (WB), and primary fibroblast

isolation/culture as needed for different experiments. Normal skin samples were obtained either from residual skin discarded during surgery or from clinically normal skin adjacent to benign lesions. Detailed clinical information for these samples is listed in Table S1. The integrative single-cell transcriptomic analysis dataset was constructed using the three HTS samples generated in our laboratory and NS samples obtained from GSE186476 and an additional publicly available dataset (GSE156326). For cross-disease validation, the independent keloid scRNA-seq dataset GSE163973, comprising three keloid and three normal scar samples, was analyzed separately.

Single-cell RNA-seq data processing

Single-cell RNA-seq datasets were processed in R using Seurat (v4.4.0) [31]. All the newly generated data and those from public datasets were processed using the same Seurat-based workflow to reduce analysis-related variations. Cells considered low quality were removed according to the following filtering thresholds: fewer than 200 detected genes, more than 4000 detected genes, or a mitochondrial transcript content exceeding 10%. Following quality filtering, the expression matrices were normalized and subjected to log transformation, and the top 3000 highly variable genes were retained for downstream analyses. Principal component analysis was carried out with the RunPCA function, and intersample and interdataset batch variation was corrected using Harmony [32]. Cell identities were assigned on the basis of CellMarker 2.0 in combination with previously reported canonical markers. Fibroblasts were subsequently extracted for reclustering analysis. Differentially expressed genes across fibroblast subsets were identified and ranked for gene set enrichment analysis (GSEA). In addition, pseudotime analysis was conducted using Monocle 2, whereas intercellular communication networks were inferred with CellChat [33, 34].

Spatial transcriptomic data analysis

Spatial transcriptomic data from NS samples were obtained from GSE225475. Data preprocessing, including normalization, scaling, and feature extraction, was performed in Seurat. Subsequent analyses were carried out on the basis of the spatial expression patterns of genes of interest.

SMR analysis

Summary data–based Mendelian randomization (SMR) was applied to investigate the relationships between gene expression and complex traits. The HEIDI test was further used to discriminate signals potentially driven by pleiotropy or causality from those attributable to associations [35]. For each gene, the leading *cis*-eQTL was chosen as the instrumental variable. Significant *cis*-eQTLs were defined as those with a PeQTL $<5.0 \times 10^{-8}$, indicating a significant genome-wide association with gene expression, and a minor allele frequency (MAF) > 0.01 to ensure sufficient allele representation in the population. The HEIDI test threshold of PHEIDI >0.05 was applied to reduce the likelihood that observed SMR associations were driven by associations between distinct causal variants. eQTL summary data were obtained from the GTEx v8 resource for "Skin—Not Sun Exposed (Suprapubic)," whereas keloid GWAS summary statistics were retrieved from BioBank Japan (ID: bbj-a-131). Candidate genes associated with endoplasmic reticulum stress were prioritized by combining the SMR results with additional bioinformatics evidence.

CUT&Tag sequencing and library preparation

CUT&Tag assays were carried out to map RUNX1 occupancy in hypertrophic scar fibroblasts (HTSFs). Library preparation was performed using a NovoNGS 2.0 kit (Novoprotein, China) according to the manufacturer's protocol. Briefly, 1×10^5 cells per sample were immobilized on ConA-coated magnetic beads and incubated sequentially with an anti-RUNX1 primary antibody (25315-1-AP; Proteintech) and the corresponding secondary antibody. After the samples were washed, pA-Tn5 transposase was added, followed by tagmentation at 37°C for 1 h in the presence of $MgCl_2$. DNA fragments were then released by proteinase K digestion and purified for subsequent library construction. The library concentration was quantified with a Qubit 4 fluorometer, and the final libraries were subjected to 150-bp paired-end sequencing on a NovaSeq platform (Novogene, China).

CUT&Tag–qPCR

CUT&Tag–qPCR was performed to confirm RUNX1 enrichment at selected candidate regions identified from the CUT&Tag peak profiles together with motif prediction. CUT&Tag was carried out as described above, and the purified DNA fragments obtained from the si-NC, si-RUNX1, and IgG groups were used as templates for quantitative polymerase chain reaction (qPCR). Quantitative real-time PCR was performed on a Bio-Rad real-time PCR system using SYBR Green-based detection. The enrichment of each target region is expressed as the relative enrichment, with the si-NC group used as the reference and the IgG group serving as the negative control. The sequences of the primers used for CUT&Tag–qPCR are listed in Table S2.

RNA sequencing and bioinformatics analysis

Total RNA was isolated from HTSFs in the RUNX1 knockdown group, the BBR-treated group, and their matched control groups using TRIzol reagent. RNA integrity and quality were evaluated using an Agilent 2100 Bioanalyzer, and only samples whose RNA integrity number (RIN) was greater than 7.0 were used for library preparation. In brief, poly(A) + mRNA was enriched with oligo(dT) magnetic beads and then fragmented under elevated temperature. First-strand cDNA was synthesized using random primers, followed by second-strand synthesis to generate strand-specific libraries incorporating deoxyuridine triphosphate (dUTP). After end repair, adaptor ligation, and uracil-DNA glycosylase (UDG) digestion of the uracil-containing strand, the libraries were completed and prepared for sequencing. Libraries with an average insert size of ~300 bp were sequenced on the Illumina NovaSeq 6000 platform by LC-Bio Technology.

For the bioinformatics analysis, raw sequencing reads were first filtered using fastp. The resulting clean reads were aligned to the

human reference genome (GRCh38) with HISAT2. Gene-level raw counts were generated through transcript assembly and quantification using StringTie and subsequently used for differential expression analysis. Differentially expressed genes were identified with DESeq2, and those with a *P*-value $<.05$ were considered to be significantly differentially expressed. Functional enrichment analyses, including Gene Ontology (GO), Kyoto Encyclopedia of Genes and Genomes (KEGG), and GSEA, were performed using the clusterProfiler package in R to characterize the transcriptomic changes associated with RUNX1 silencing and BBR treatment in HTSFs.

Virtual screening and molecular docking

The POSTN protein structure was used as the receptor for the virtual screen. Small-molecule compounds from the Traditional Chinese Medicine Systems Pharmacology Database and Analysis Platform (TCMSP) were screened using AutoDock Vina. Candidate compounds were ranked according to their predicted binding affinity, and BBR was selected for subsequent analyses on the basis of both its docking performance and prior pharmacological evidence. The predicted binding mode was then visualized to assess the interaction between BBR and the putative binding pocket of POSTN.

Molecular dynamics simulations

Molecular dynamics simulation of the POSTN–BBR complex was performed for 100 ns using the GROMACS software package. The root mean square deviation (RMSD), root mean square fluctuation (RMSF), and radius of gyration (Rg) were determined to evaluate the structural stability, residue-level flexibility, and the overall compactness of the complex, respectively. An analysis of hydrogen bonds was further performed to assess the stability of the interactions between POSTN and BBR throughout the simulation. In addition, principal component analysis and free energy landscape analysis were conducted to characterize the conformational dynamics and low-energy states of the POSTN–BBR complex. Low-affinity control compounds with available structural and docking data were selected from the same TCMSP-to-POSTN screening and evaluated using the same molecular dynamics and MM-GBSA protocols as the POSTN–BBR complex.

Cell culture

Human HTSFs and normal skin fibroblasts (NSFs) were established from tissue explants using the explant outgrowth method. Briefly, fresh tissue samples were rinsed three times in PBS supplemented with 1% penicillin–streptomycin. After careful removal of subcutaneous fat and other impurities, the dermal fragments were cut into small pieces and transferred to complete culture medium for primary culture. Cells from passages 3 to 5 were used for subsequent experiments to ensure relatively stable cellular phenotypes. Human umbilical vein endothelial cells (HUVECs) were cultured in Dulbecco's modified Eagle medium (DMEM) supplemented with 10% fetal bovine serum and 1% penicillin–streptomycin. All the cells were maintained at 37°C in a humidified incubator with 5% CO_2.

Transient transfection

Transient transfection of cells was carried out with Lipofectamine 3000 (Invitrogen, USA) according to the manufacturer's instructions. The RUNX1-targeting siRNA oligonucleotides used were as follows: si-RUNX1#1, sense 5′-GCACUCUGGUCACUGUGAUTT-3′ and antisense 5′-AUCACAGUGACCAGAGUGCTT-3′; and si-RUNX1#2, sense 5′-CCAUCACUGUCUUCACAAATT-3′ and antisense 5′-UUUGUGAAGACAGUGAUGGTC-3′. The POSTN-targeting siRNA sequences used were as follows: si-POSTN#1, sense 5′-CACUGUUAAUUGUGCUCGATT-3′ and antisense 5′-UCGAGCACAAUUAACAGUGTT-3′; and si-POSTN#2, sense 5′-GCACUUGUAAGAACUGGUATT-3′ and antisense 5′-UACCAGUUCUUACAAGUGCTT-3′. The ATF4-targeting siRNA sequences were as follows: si-ATF4, sense 5′- UUCUCUAGAUGGCCGAUCUTT-3′ and antisense 5′-AGAUCGGCCAUCUAGAGAATT-3′; nonspecific scrambled siRNA served as the negative control. RUNX1, GPX4, and ATF4 overexpression plasmids were constructed by Tsingke Biotechnology (Beijing, China) and used for subsequent overexpression experiments.

Quantitative real-time PCR

Total RNA was isolated from cells or tissues using TRIzol reagent according to the manufacturer's protocol. Equal amounts of RNA were reverse-transcribed into cDNA using PrimeScript RT Master Mix (Yeasen). Quantitative real-time PCR was then carried out on a Bio-Rad real-time PCR system using SYBR Green–based detection. The relative mRNA levels of the indicated genes were normalized to those of Glyceraldehyde-3-phosphate dehydrogenase (GAPDH) as the internal control and calculated using the $2^{-\Delta\Delta Ct}$ method. The results are presented as fold changes relative to the corresponding control group. The sequences of primers used in this study are listed in Table S3.

Cell viability assay

A Cell Counting Kit-8 (CCK-8; AbMole, China) assay was used to evaluate cell viability. HTSFs were plated in 96-well plates at 5×10^3 cells per well and then treated as indicated for 48 h. After treatment, the medium in each well was replaced with 100 μl of freshly prepared medium supplemented with 10% CCK-8 solution, followed by incubation at 37°C for 1 h. The absorbance value at 450 nm was subsequently measured with a microplate reader.

Wound healing assay

A wound healing assay was performed to evaluate the migratory capacity of the HTSFs. Treated cells were plated in 6-well plates, and a linear wound was generated in the center of each well with a sterile 200 μl pipette tip once the cells approached 90% confluence. After the detached cells were removed by washing with PBS, the remaining cells were maintained in serum-reduced medium. Images were obtained at 0 and 24 h after scratching, and wound closure was analyzed using ImageJ software.

Transwell assay

A 24-well Transwell system with 8 μm pore membranes (Corning, USA) was used to evaluate cell migration. A total of 5×10^3 cells

suspended in 200 μl of serum-free DMEM were added to the upper chamber, and 500 μl of DMEM containing 10% Fetal bovine serum (FBS) was added to the lower chamber as a chemoattractant. After incubation, the cells on the upper surface of the membrane were removed with a cotton swab, whereas the cells that had migrated to the lower surface were fixed, stained with crystal violet, photographed under a microscope, and counted.

EdU proliferation assay

A Click-iT EdU Cell Proliferation Detection Kit (Beyotime, China) was used to assess cell proliferation. When the cells reached nearly 70% confluence, EdU was added to the medium at a final concentration of 10 μM, and the cells were incubated for 12 h at 37°C. The cells were subsequently fixed with 4% paraformaldehyde, permeabilized in 0.3% Triton X-100, and subjected to a click reaction in the dark following the manufacturer's instructions. After the nuclei were counterstained with Hoechst, fluorescence images were captured, and the proportion of EdU-labeled cells was analyzed using ImageJ.

Collagen gel contraction assay

HTSF contractility was examined using a collagen gel contraction model. Cells were suspended in collagen working solution, and 500 μl of the suspension was dispensed into each well of 24-well plates (Cell Biolabs, USA). After the gels had fully solidified, they were gently loosened from the well boundaries to enable spontaneous contraction. Images of the same gels were recorded at 0, 24, and 48 h, and the gel area at each time point was quantified using ImageJ. The contraction ratio was calculated relative to the initial gel area at 0 h using the following formula: contraction ratio (%) = $[(A_0 - A_t)/A_0] \times 100$, where A_0 and A_t represent the gel areas at 0 h and time t, respectively.

Apoptosis analysis

Apoptosis was quantified with an Annexin V-FITC (fluorescein isothiocyanate)/PI (propidium iodide) Apoptosis Detection Kit (BioLegend, USA). Following the indicated treatments, the HTSFs were harvested and pelleted by centrifugation and then resuspended in 100 μl of binding buffer. Annexin V-FITC (5 μl) and PI (10 μl) were then added to each sample, and staining was allowed to proceed for 15 min at room temperature in the dark. The stained cells were immediately subjected to flow cytometric detection, and the percentage of apoptotic cells was subsequently determined.

Cell cycle analysis

The cell cycle distribution was assessed using a cell cycle analysis kit (Beyotime, China). After treatment, the cells were collected, washed with PBS, and fixed in precooled 75% ethanol at −20°C for 24 h. After removal of the fixative, the cells were resuspended in PI staining solution according to the manufacturer's instructions and incubated in the dark for 30 min. Flow cytometry (BD Biosciences, USA) was then performed to determine the cell cycle profiles, and the proportions of cells in the G1, S, and G2 phases were calculated.

HUVEC functional assays and conditioned medium treatment

Conditioned medium (CM) was collected from HTSFs subjected to different treatments, followed by centrifugation to remove cell debris. For the rescue experiments, recombinant human MDK (R&D Systems) was added to the corresponding CM. HUVECs were subsequently cultured with the appropriate CM and subjected to migration, proliferation, and angiogenic activity assays. To analyze tube formation, HUVECs were plated into Matrigel-precoated 24-well plates (Corning, USA) and maintained in the indicated CM. The formation of capillary-like networks was observed microscopically, and both the number of branch points and total tube length were quantified with ImageJ software.

Reactive oxygen species measurements

To detect intracellular reactive oxygen species (ROS) levels, HTSFs were first plated in 6-well plates at a density of 1.2×10^6 cells per well. After 48 h of treatment, the cells were incubated with 10 μM DCFH-DA working solution (Beyotime, China) diluted in serum-free medium at 37°C for 20 min. The excess probe was removed by washing the cells, after which the fluorescence signals were detected by flow cytometry (Beckman, USA). The measured fluorescence intensity was used to indicate total intracellular ROS accumulation.

Lipid ROS measurements

Lipid peroxidation levels were evaluated using the fluorescent probe Liperfluo (Dojindo, Japan). Following treatment, the HTSFs were collected and exposed to Liperfluo working solution at 37°C in the dark. After staining, the cells were washed and analyzed by flow cytometry (Beckman, USA). The green fluorescence intensity was measured, and the mean fluorescence intensity was taken as an indicator of the intracellular lipid ROS concentration.

Malondialdehyde assay

Intracellular malondialdehyde (MDA) levels were measured using an MDA assay kit (Nanjing Jiancheng, China). After treatment, the HTSFs were collected, lysed, and homogenized. On the basis of the reaction between MDA and thiobarbituric acid under acidic high-temperature conditions, the absorbance was measured using a microplate reader (Bio-Rad, USA). The MDA levels were normalized to the total protein concentration.

Detection of intracellular Fe^{2+}

Intracellular ferrous iron was detected using a FerroOrange fluorescent probe (Dojindo, Japan). Following the indicated treatments, the cells were rinsed with serum-free medium and then incubated with FerroOrange working solution at 37°C in the dark. The fluorescence signals were subsequently measured using a multifunctional microplate reader (Bio-Rad, USA), and the resulting intensity values were taken as an indicator of intracellular Fe^{2+} accumulation.

Intracellular glutathione measurements

The intracellular content of reduced glutathione (GSH) was quantified with a commercial GSH assay kit (Nanjing Jiancheng, China). After treatment, the HTSFs were harvested and lysed by sonication. The subsequent colorimetric reaction was carried out in accordance with the manufacturer's protocol, and the absorbance was measured with a microplate reader (Bio-Rad, USA). The final GSH values were normalized to the total protein concentration.

Mitochondrial membrane potential assay

Changes in the mitochondrial membrane potential were examined using a JC-1 fluorescent probe (Beyotime, China). After treatment, the HTSFs were stained with JC-1 working solution in the dark. Under conditions of high mitochondrial membrane potential, JC-1 accumulates in mitochondria as red fluorescent aggregates, whereas a reduction in membrane potential leads to the predominance of its green fluorescent monomeric form. Following Hoechst counterstaining of the nuclei, fluorescence images were captured with a confocal microscope, and the mitochondrial status was evaluated on the basis of the ratio of red to green fluorescence.

Histological staining and immunohistochemistry

Skin tissue samples were fixed, embedded in paraffin, and cut into 4 μm sections for hematoxylin and eosin (H&E), Masson's trichrome, and Sirius Red staining. For immunohistochemical analysis, the paraffin sections were first deparaffinized with xylene and rehydrated through a graded ethanol series, followed by antigen retrieval in Tris-Ethylenediaminetetraacetic acid (EDTA) buffer (pH 9.0). After blocking nonspecific binding with 5% goat serum, the sections were incubated overnight at 4°C with an anti-RUNX1 primary antibody (1:600; 25315-1-AP; Proteintech). The following day, the sections were incubated with an Horseradish peroxidase (HRP)-conjugated secondary antibody (1:2000, ab205718, Abcam) for 60 min at room temperature. After the sections were washed with PBS, signals were developed using a DAB kit (DAKO, Denmark), and the nuclei were counterstained with hematoxylin. Whole-slide sections were digitized using a NanoZoomer S360 digital slide scanner (Hamamatsu Photonics, Japan) at 20$\times$ magnification under identical scanning settings across comparable groups. Representative regions and the corresponding enlarged images were selected for figure presentation. For quantitative analysis, five randomly selected nonoverlapping fields from comparable tissue regions of each section were analyzed using ImageJ. The area with positive staining for RUNX1 was determined using the same fixed threshold for all the images and normalized to the total tissue area within each field.

Western blotting

Total protein from cultured cells and tissue samples was prepared using Radioimmunoprecipitation assay (RIPA) lysis buffer supplemented with protease inhibitors. Protein abundance was quantified with a Bicinchoninic acid (BCA) protein assay kit (Beyotime, China). Equivalent amounts of protein were then resolved by Sodium dodecyl sulfate–polyacrylamide gel electrophoresis (SDS-PAGE) and electrotransferred to Polyvinylidene difluoride (PVDF) membranes (Millipore, USA). The membranes were blocked in 5% skim milk for 1 h at room temperature and then incubated overnight at 4°C with the following primary antibodies: anti-RUNX1 (1:5000, 25315-1-AP, Proteintech), anti-MMP2 (1:500, 10373-2-AP, Proteintech), anti-MMP9 (1:1000, 10375-2-AP, Proteintech), anti-TGF-β1 (1:500, ab215715, Abcam), anti-ATF4 (1:500, 10835-1-AP, Proteintech), anti-phospho-eIF2α (1:5000, 68023-1-Ig, Proteintech), anti-PERK (1:400, 24390-1-AP, Proteintech), anti-phospho-PERK (1:500, 29546-1-AP, Proteintech), anti-BiP (1:2000, 11587-1-AP, Proteintech), anti-SLC7A11 (1:1000, 26864-1-AP, Proteintech), anti-GPX4 (1:500, 67763-1-Ig, Proteintech), anti-POSTN (1:5000, 66491-1-Ig, Proteintech), anti-COL III (1:500, 22734-1-AP, Proteintech), anti-COL I (1:500, 14695-1-AP, Proteintech), α-SMA (1:5000, 67735-1-Ig, Proteintech), and anti-GAPDH (1:5000, 60004-1-Ig, Proteintech). After being washed with Tris-buffered saline with Tween 20 (TBST), the membranes were incubated with HRP-conjugated secondary antibodies for another hour at room temperature. The protein bands were then detected using an Enhanced chemiluminescence (ECL) substrate (Tanon, China).

Animal models

Animal experiments were conducted following approval from the Animal Ethics Committee of the Fourth Military Medical University (approval no. 20250121) and in accordance with the Guide for the Care and Use of Laboratory Animals. Male C57BL/6 mice aged 8 weeks and male New Zealand White rabbits weighing 3.0–4.0 kg were obtained from the Experimental Animal Center of the Fourth Military Medical University. In accordance with the study design, three animal models were established, namely, a bleomycin-induced skin fibrosis mouse model, a mouse scar model, and a rabbit ear hypertrophic scar model. The first two models were mainly used to validate the role of RUNX1 in skin fibrosis and scar formation *in vivo*, whereas the rabbit ear hypertrophic scar model was used to evaluate the antiscar therapeutic potential of BBR. Lesion thickness, collagen deposition, and alterations in the expression of related proteins were examined by histological staining, immunohistochemistry, and immunofluorescence.

A bleomycin-induced skin fibrosis model was established to determine whether RUNX1 silencing could attenuate fibrotic remodeling *in vivo* [36, 37]. Briefly, 8-week-old male C57BL/6 mice received a single subcutaneous injection of AAV9-ctrl or AAV9-shRUNX1 (PackGene, China) into the dorsal skin 21 days before the initiation of bleomycin treatment according to the study design. Skin fibrosis was then induced by daily subcutaneous injection of bleomycin (Thermo Fisher, R25001; 100 μg/100 μl in PBS) into the dorsal skin for 21 consecutive days, whereas control mice received an equivalent volume of PBS. The mice were sacrificed at the end of the 21-day bleomycin treatment period, and dorsal skin tissues were collected for histological analyses, including H&E, Masson's trichrome, and Sirius Red staining. The expression of RUNX1, POSTN, α-SMA, ATF4, and GPX4 was further evaluated by IHC and IF.

A mouse mechanical tension-induced scar model was used to assess whether RUNX1 silencing could attenuate scar formation *in vivo* [38]. Briefly, 8-week-old male C57BL/6 mice were subcutaneously injected with AAV9-ctrl or AAV9-shRUNX1 into the dorsal skin 21 days before the surgical procedure. On the day of surgery, the dorsal hair was removed by shaving, followed by

topical depilation for 30 s. A single circular full-thickness wound (6 mm in diameter) was generated on the dorsal skin with a biopsy punch. A silicone splint was then positioned around the wound and fixed with interrupted sutures and cyanoacrylate adhesive to limit wound contraction and maintain local mechanical tension during repair. The mice were sacrificed 14 days after surgery, and scar tissue was harvested for further analysis. The scar elevation index was determined, and scar thickness and collagen accumulation were assessed by H&E and Masson's trichrome staining. RUNX1 expression was analyzed by immunohistochemistry, whereas ATF4, GPX4, α-SMA, and POSTN expression was evaluated by immunofluorescence staining.

A rabbit ear hypertrophic scar model was used to evaluate the antiscar therapeutic potential of BBR. This model was established according to our previously published protocol [39]. Briefly, New Zealand White rabbits were anesthetized with sodium pentobarbital, and the hair on the ventral surface of the ears was removed by shaving followed by chemical depilation. Four circular full-thickness wounds (each 10 mm in diameter) were created on the ventral aspect of each ear using a biopsy punch, and the perichondrium within each wound was carefully removed to establish the scar model. Seven days after wounding, the crust covering the wounds was gently removed to re-expose the wound bed. After scar formation occurred, the animals were treated according to the experimental design. As indicated in the study timeline, vehicle or BBR was administered locally by subcutaneous injection at the scar site once every 3 days beginning on postoperative Day 20 for a total of six injections. The animals were euthanized at the experimental endpoint, and scar tissue was harvested for subsequent analyses. Histological changes and collagen deposition were evaluated by H&E and Masson's trichrome staining, and α-SMA expression was assessed by immunofluorescence staining. Scar thickness was also quantified.

For AAV administration, each mouse received a subcutaneous injection of 1×10^{11} viral particles of either AAV9-shRUNX1 or AAV9-ctrl into the dorsal skin 21 days prior to surgery. Twelve mice were then randomly divided into AAV9-shRUNX1 and AAV9-ctrl groups.

Statistical analysis

Statistical analyses were performed using GraphPad Prism 10.1 and R version 4.3.0. The normality of data distribution was assessed using the Shapiro–Wilk test. For comparisons between two independent groups, a two-tailed *t*-test was used for normally distributed data, whereas the Mann–Whitney *U* test was used for non-normally distributed data. For matched samples, a paired two-tailed *t*-test was used when the paired differences were normally distributed. For comparisons among three or more groups, ordinary one-way ANOVA followed by Tukey's multiple-comparisons test or the Kruskal–Wallis test followed by Dunn's multiple-comparisons test was used as appropriate. Correlations were assessed using Pearson's or Spearman's correlation analysis, as indicated in the corresponding figure legends. IC50 values were determined by nonlinear regression. The number of biological replicates for each assay is indicated in the corresponding figure legends. A *P*-value <0.05 was considered statistically significant. "ns" denotes that there is no significant difference, whereas *, **, and *** represent $P < 0.05$, $P < 0.01$, and $P < 0.001$, respectively.

Results

Integrated single-cell transcriptomics reveals the cellular landscape of hypertrophic scar and normal skin

To characterize the overall cellular composition of HTS, we integrated single-cell transcriptomic datasets from HTS and normal skin for unified analysis. The integrated cellular atlas resolved nine major cell types, including smooth muscle cells (SMCs), endothelial cells (ECs), fibroblasts (FBs), keratinocytes (KCs), T cells, macrophages (Macs), melanocytes (Mels), Schwann cells (SCs), and mast cells (Figure S1a). These annotations were supported by the expression patterns of canonical marker genes, including COL1A1, KRT14, PTPRC, AIF1, VWF, ACTA2, MITF, S100b, and CTSG (Figure S1c and d). Proportional analysis revealed no obvious difference in the distribution of major cell types between the two groups (Figure S1b), suggesting that the key pathological alterations in HTS may be attributable to functional reprogramming within specific cell populations. Given the central role of fibroblasts in extracellular matrix deposition in HTS, we extracted all the fibroblasts for dimensional reduction and clustering analysis, which revealed five subclusters with distinct transcriptional features (Clusters 0–4) (Figure 1a). Proportional analysis revealed significant differences in fibroblast subcluster distribution between NS and HTS tissue. Notably, Cluster 4 was nearly absent in normal skin but was significantly expanded in HTS, suggesting that this subpopulation may represent a key disease-associated fibroblast subset involved in scar progression (Figure 1c).

RUNX1 is enriched in a POSTN+ fibroblast subpopulation in HTS and related skin fibrotic disorders

To define the molecular characteristics of the above pathogenic fibroblast subset, we analyzed genes that were differentially expressed across fibroblast subclusters. A bubble plot analysis revealed that Cluster 4 was characterized by high expression of POSTN, SFRP4, COMP, and the transcription factor RUNX1 (Figure 1b). Violin plots further revealed that, compared with the other subclusters, Cluster 4 not only exhibited significantly elevated expression of the activated stromal marker POSTN but also displayed a stronger capacity to produce ECM, with high levels of COL1A1 and COL3A1, while RUNX1 expression peaked in this cluster (Figure 1d). These findings suggest that Cluster 4 represents a strongly activated RUNX1-high POSTN+ profibrotic fibroblast population. Spatial transcriptomic analysis revealed that, in normal skin, the spatial distribution of RUNX1 overlapped with that of fibroblast-associated regions, supporting its stromal localization (Figure 1e). Pseudotime analysis further revealed that RUNX1 expression gradually increased as the fibroblasts progressed toward a terminal pathological state (Figure 1f). Functional enrichment analysis revealed that HTS-derived Cluster 4 cells were enriched not only in matrix remodeling pathways such as ECM–receptor interactions but also specifically in protein processing in the endoplasmic reticulum (Figure 1g). Together, these findings suggest that RUNX1 may participate in the

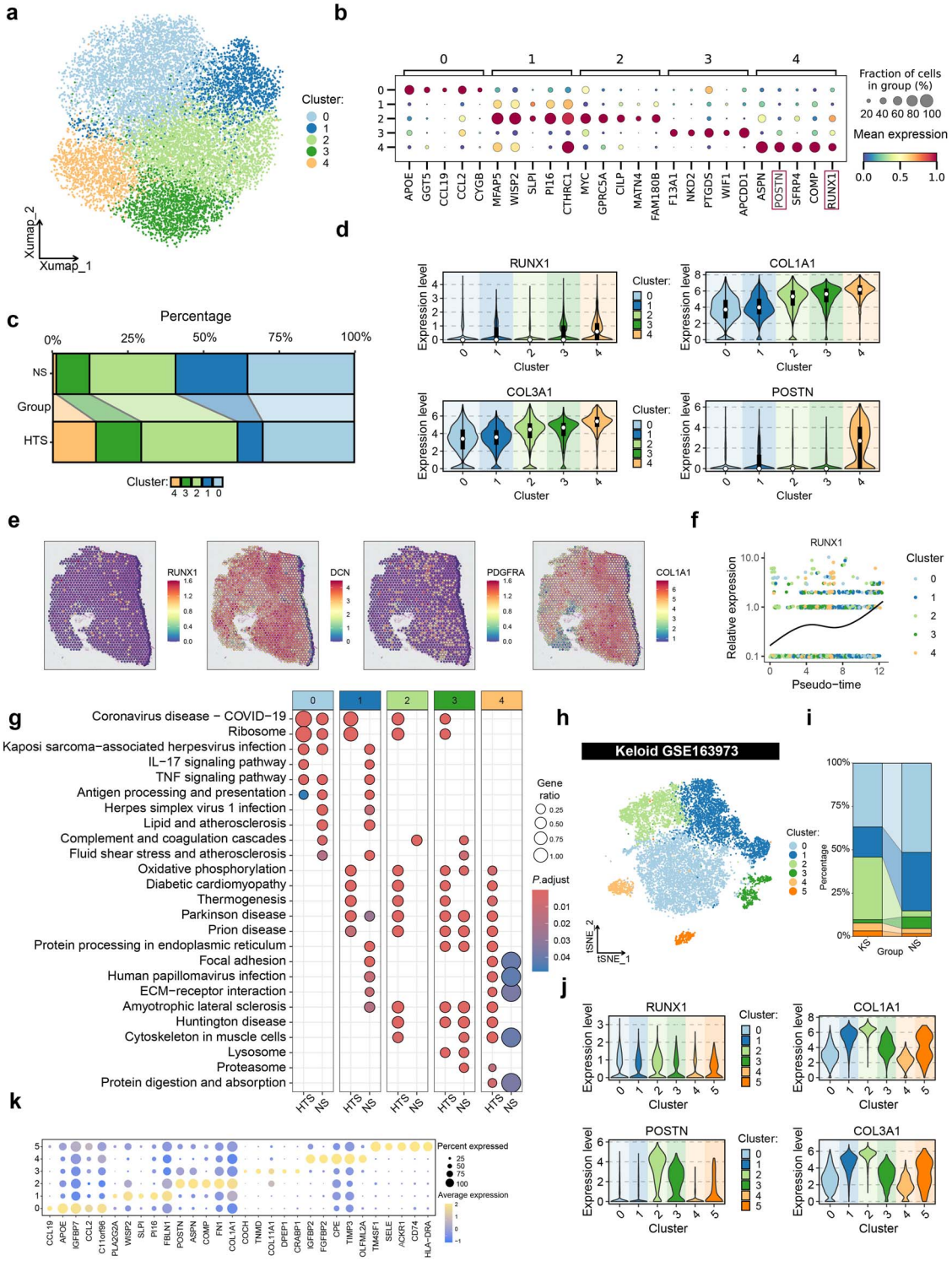


Figure 1 Fibroblast reclustering reveals a RUNX1-enriched POSTN+ activated subpopulation in hypertrophic scar and related skin fibrosis disorders. (**a**) UMAP plot of re-clustered fibroblasts, showing five fibroblast subpopulations with distinct transcriptional features in HTS and NS. (**b**) Dot plot showing the marker genes of each fibroblast subpopulation in the HTS dataset. (**c**) Comparison of the relative proportions of fibroblast subpopulations between NS and HTS. (**d**) Violin plots showing the distribution of RUNX1, COL1A1, COL3A1, and POSTN across fibroblast subpopulations in the HTS dataset. (**e**) Spatial feature plots of RUNX1 and fibroblast marker genes (DCN, PDGFRA, and COL1A1). (**f**) Pseudotime analysis of fibroblasts showing the dynamic expression changes of RUNX1 along cell state progression in the HTS dataset. (**g**) KEGG pathway enrichment analysis of fibroblast subpopulations in the HTS dataset. (**h**) tSNE plot of re-clustered fibroblasts from the independent keloid single-cell RNA-seq dataset (GSE163973). (**i**) Comparison of the relative proportions of fibroblast subpopulations between the two groups. (**j**) Violin plots showing the distribution of RUNX1, COL1A1, COL3A1, and POSTN across fibroblast subpopulations in the keloid dataset. (**k**) Dot plot showing the marker genes of each fibroblast subpopulation in the keloid dataset. *HTS* hypertrophic scar, *NS* normal skin, *UMAP* uniform manifold approximation and projection, *t-SNE* t-distributed stochastic neighbor embedding

sustained activation of POSTN+ fibroblasts and is closely associated with ER stress–related adaptive programs. To determine whether this association was preferential to RUNX1 within the RUNX family, we examined RUNX2 and RUNX3 expression across fibroblast subclusters. RUNX2 and RUNX3 showed lower or less consistent expression, whereas in FB4, 51.3% of the cells were positive for RUNX1, whereas RUNX2-positive cells accounted for 22.0% of the cells and RUNX3-positive cells accounted for 0.9% (Figure S2a and b). These findings support the prioritization of RUNX1 as the RUNX family member most prominently associated with the POSTN+ fibroblast state. However, this comparison was intended to establish the relative prioritization of RUNX1 rather than to exclude potential context-dependent roles of RUNX2 or RUNX3 within fibroblast populations.

To further assess whether a similar fibroblast state could also be observed in another fibrotic skin disorder, we additionally analyzed the independent keloid scRNA-seq dataset GSE163973. Analysis of this dataset identified the major cell populations, including endothelial cells, fibroblasts, pericytes/smooth muscle cells, keratinocytes, myeloid cells, mast cells, Schwann cells, lymphoid cells, and melanocytes (Figure S3a). These annotations were supported by the expression of canonical marker genes, including VWF, COL1A1, RGS5, KRT14, LYZ, MITF, TPSAB1, PTPRC, and S100b (Figure S3b). Proportional analysis further showed differences in the overall cellular composition between the two groups (Figure S3c). We next extracted fibroblasts and performed re-clustering analysis, which identified six fibroblast subpopulations (Figure 1h). Notably, Cluster 2 was preferentially represented in keloid tissue (Figure 1i). Violin plot analysis revealed that Cluster 2 was characterized by high POSTN expression together with relatively elevated RUNX1 expression, whereas COL1A1 and COL3A1 were more broadly distributed across matrix-producing fibroblast populations (Figure 1j). Consistently, dot plot analysis revealed that Cluster 2 expressed POSTN together with multiple fibrosis-associated markers, supporting its annotation as an activated POSTN+ fibroblast subset (Figure 1k). Further marker expression analysis revealed that POSTN-high Cluster 4 in the integrated HTS dataset and POSTN-high Cluster 2 in the independent keloid dataset GSE163973 coexpressed COL1A1, FAP, THY1, and ACTA2 and exhibited the highest percentages of cells positive for these markers among their respective fibroblast subclusters (Figure S4a and b), supporting their annotation as activated POSTN+ fibroblast states across the analyzed datasets. These findings indicate that a similar RUNX1-high POSTN+ fibroblast state is also present in keloid and provide additional cross-disease single-cell support that preferential RUNX1 enrichment in POSTN+ activated fibroblasts may represent a shared feature of skin fibrosis. To assess whether the RUNX1-high POSTN+ fibroblast state could be recovered within a published HTS cohort itself, we separately reanalyzed the public HTS scRNA-seq dataset GSE156326. Consistent with the results of our integrated analysis, a POSTN-high fibroblast population was identifiable in GSE156326 and showed stable enrichment of RUNX1 expression, with increased representation in HTS compared with that in NS (Figure S5a–c). Quantification of the POSTN-positive and RUNX1-positive cell fractions across fibroblast subpopulations further supported the coenrichment of these markers in the corresponding fibroblast state (Figure S5d). These findings support the conservation of the RUNX1-high POSTN+ fibroblast state across local and published HTS scRNA-seq cohorts.

RUNX1 is consistently upregulated in skin fibrosis disorders and is associated with matrix remodeling

Because single-cell analysis suggested that RUNX1 may participate in the pathological activation of POSTN+ fibroblasts, we evaluated the expression pattern of RUNX1 across skin fibrosis disorders and its association with matrix remodeling programs. Analysis of multiple public transcriptomic datasets revealed increased fibrosis-related scores for collagen, ECM, glycoproteins, and proteoglycans in hypertrophic scar (GSE181540 and OEP002674), keloid (GSE280420 and GSE212954), and systemic sclerosis (GSE130955), accompanied by increased RUNX1 expression (Figure 2a–e). Correlation analysis further showed positive associations between RUNX1 expression and ECM scores across multiple independent cohorts, supporting a close link between RUNX1 and matrix remodeling programs in fibrotic skin diseases (Figure 2f).

We next detected RUNX1 expression in various fibrotic animal models and human fibrosis disease samples *in vivo*. Immunohistochemical staining revealed that, compared with those in normal skin, RUNX1-positive signals were significantly increased in both bleomycin-induced fibrotic skin and the hypertrophic scar mouse model (Figure 2g–i). Histological validation using H&E and Masson's trichrome staining confirmed the presence of dermal remodeling and collagen deposition in the mouse hypertrophic scar model and bleomycin-induced skin fibrosis model (Figure S6). WB analysis of clinical samples revealed that RUNX1 protein expression was significantly elevated in both HTS and KS tissues compared with that in NS (Figure 2j and k). Histological staining of clinical tissues also revealed typical fibrotic changes in HTS and KS, including dermal thickening and dense, disorganized collagen deposition, together with significantly increased RUNX1 immunostaining intensity (Figure 2l and m). Together, these findings support a close association between RUNX1 and matrix remodeling across skin fibrosis disorders.

RUNX1 silencing suppresses the activated and profibrotic phenotype of HTSFs

Given that functional investigations across the full spectrum of skin fibrosis disease are not readily feasible, we used HTSFs as a representative model to explore the role of RUNX1 in fibrotic fibroblast activation and silenced RUNX1 using two independent siRNAs. WB analysis confirmed that both siRNAs significantly reduced RUNX1 protein expression (Figure 3a and Figure S7a). EdU assays revealed that both si-RUNX1#1 and si-RUNX1#2 significantly reduced the proportion of EdU-positive HTSFs, indicating impaired proliferative activity (Figure 3b and c). Wound healing and Transwell assays demonstrated that RUNX1 silencing significantly suppressed HTSF migration (Figure 3d–g). Time-course collagen gel contraction assays revealed that RUNX1 silencing significantly reduced HTSF-mediated matrix contraction at 24 and 48 h, with contraction ratios calculated relative to the corresponding initial gel area at 0 h (Figure 3h and i). Flow cytometric analysis revealed that RUNX1 silencing increased the proportion of cells in the G1 phase and decreased the proportion of cells in the S phase (Figure 3j), whereas Annexin V/PI staining indicated

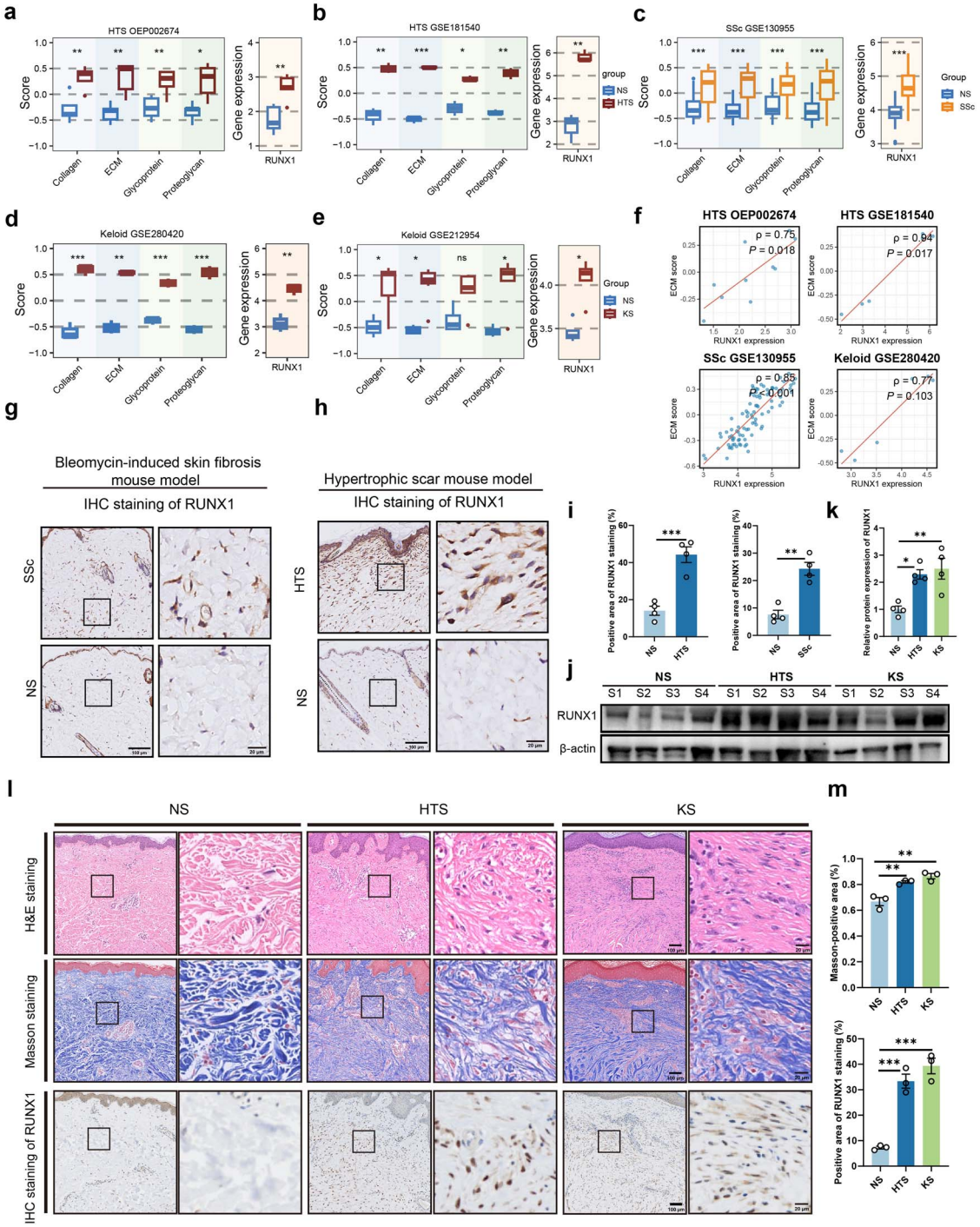


Figure 2 RUNX1 is upregulated in both animal and human skin fibrosis disorders and is associated with matrix remodeling. (**a**–**e**) Comparison of collagen-, ECM-, glycoprotein-, and proteoglycan-related scores, as well as RUNX1 expression levels, in HTS, KS, and SSc samples from the indicated public transcriptomic datasets. (**f**) Correlation analysis between RUNX1 expression and ECM scores across different public datasets. (**g**, **h**) IHC staining showing RUNX1 expression in bleomycin-induced mouse skin fibrosis and hypertrophic scar mouse models. Enlarged views of the boxed regions are shown on the right. Scale bar: 100 μm; 20 μm. (**i**) Quantification of RUNX1-positive staining area in the indicated mouse models, normalized to the total tissue area within each field. $n = 4$ mice per group. (**j**, **k**) Western blot analysis and quantification of RUNX1 protein expression in clinical NS, HTS, and KS tissues. $n = 4$ independent human samples per group. (**l**) H&E staining, Masson staining, and RUNX1 immunohistochemistry in clinical NS, HTS, and KS tissues. Enlarged views of the boxed regions are shown on the right. Scale bar: 100 μm; 20 μm. (**m**) Quantification of Masson-positive collagen area and RUNX1-positive staining area in clinical tissues, normalized to the total tissue area within each field. $n = 3$ independent human samples per group. Data are presented as mean ± SD. Statistical analyses were performed using two-tailed *t*-tests, one-way ANOVA followed by Tukey's multiple-comparisons test, or Mann–Whitney *U* tests as appropriate after assessment of normality using the Shapiro–Wilk test. Paired *t*-tests were used for the matched samples in GSE212954. Spearman's rank correlation was used in (f). $^{*}P < 0.05$, $^{**}P < 0.01$, $^{***}P < 0.001$. *ECM* extracellular matrix, *HTS* hypertrophic scar, *KS* keloid scar, *SSc* systemic sclerosis, *NS* normal skin, *IHC* immunohistochemistry, *H&E* hematoxylin and eosin

increased apoptosis (Figure 3k). WB analysis confirmed that the expression of profibrotic molecules, including COL I, COL III, α-SMA, TGF-β1, MMP2, and MMP9, significantly decreased (Figure 3l and Figure S7b–g). Consistent with these findings, immunofluorescence staining revealed reduced α-SMA expression (Figure 3m and n). These results indicate that RUNX1 plays an important role in maintaining the activated profibrotic phenotype of HTSFs.

Integrated CUT&Tag and transcriptomic analyses identify an ATF4-associated ER stress and ferroptosis network downstream of RUNX1

To investigate the molecular basis by which RUNX1 sustains the activated HTSF phenotype, we first performed CUT&Tag sequencing in si-NC- and si-RUNX1-treated cells. Genomic annotation revealed that RUNX1-associated peaks were broadly distributed across promoters, introns, and distal intergenic regions, with a considerable fraction located in promoter-associated regions (Figure 4a). Consistent with these findings, RUNX1 silencing significantly reduced CUT&Tag signal intensity around transcription start sites (Figure 4b). Motif analysis revealed enrichment of RUNX family-related motifs together with motifs associated with stress responses and cell state regulation (Figure 4c). The functional enrichment of RUNX1-bound genes highlighted biological processes and pathways related to actin filament organization, the response to ER stress, the response to oxidative stress, protein processing in the ER, focal adhesion, and ferroptosis (Figure 4d and e).

Given these findings, we focused on ATF4 as a candidate downstream effector. GTEx analysis revealed that RUNX1 expression was positively correlated with that of ATF4 across multiple tissues and in skin tissue specifically (Figure 4g and h). Genome browser tracks revealed a clear RUNX1 binding peak at the ATF4 locus, which clearly weakened after RUNX1 was silenced (Figure 4f). Consistently, CUT&Tag–qPCR confirmed significant RUNX1 enrichment at the ATF4 promoter in si-NC cells, whereas this enrichment was substantially reduced in the si-RUNX1 group and nearly absent in the IgG control group (Figure 4i). Furthermore, the results of qPCR revealed that ATF4 mRNA expression was significantly decreased after RUNX1 knockdown (Figure 4j), suggesting that ATF4 is a direct downstream target of RUNX1.

We next performed RNA sequencing in control and si-RUNX1-transfected HTSFs. Heatmap analysis revealed that RUNX1 silencing downregulated the expression of HSPA5, ATF4, GPX4, SLC7A11, COL3A1, and COL1A1 (Figure 4k). GO and KEGG analyses revealed that the affected genes were enriched mainly in the terms "fibroblast proliferation," "extracellular matrix organization," "response to endoplasmic reticulum stress," "cellular response to oxidative stress," "protein processing in the endoplasmic reticulum," "ferroptosis," "TGF-β signaling," and "cell cycle" (Figure 4l and m). GSEA confirmed that the response to the ER stress gene set was significantly downregulated in the si-RUNX1 group (Figure 4n). In addition, qPCR validation demonstrated reduced expression of SLC7a11, HSPA5, GPX4, COL3A1, and COL1A1 after RUNX1 silencing (Figure S8a–e). Together, these data indicate that RUNX1 promotes an ATF4-associated transcriptional program linked to ER stress adaptation, ferroptosis resistance, and matrix remodeling in HTSFs.

SMR analysis and pharmacological rescue support the role of ATF4 as a downstream mediator of RUNX1

To validate the role of ATF4 downstream of RUNX1 at both the genetic and functional levels, we first compared ER stress-related signature scores across fibroblast subpopulations. Compared with the other subclusters, Cluster 4 (POSTN+ fibroblasts) had significantly higher ER stress scores (Figure 5d). Consistently, analysis of an independent keloid single-cell RNA-seq dataset revealed that the POSTN+ fibroblast subset *also* exhibited a relatively elevated ER stress score, providing additional cross-disease single-cell support for the association between POSTN+ fibroblast activation and ER stress-related adaptive programs (Figure S12a). We also performed SMR analysis by integrating GTEx skin eQTL data with keloid GWAS summary statistics from BioBank Japan. Among the ER stress-related genes examined, ATF4 showed a nominal association with keloid risk in the SMR analysis (P_SMR = 0.02258), and the HEIDI test did not detect statistically significant heterogeneity (P_HEIDI = 0.11411) (Figure 5a). Regional visualization of the ATF4 locus revealed the distributions of the local eQTL and GWAS association signals (Figure 5b), while the effect size scatter plot displayed the effects of the *cis*-eQTLs on ATF4 expression together with the corresponding effects of the GWAS on keloid risk (Figure 5c). These plots were used for descriptive visualization and were not interpreted as formal evidence of colocalization. Given that only one independent *cis*-eQTL instrument was available, these exploratory genetic findings were interpreted cautiously and considered together with the results of subsequent pharmacological rescue experiments when evaluating the role of ATF4 in RUNX1-mediated fibroblast activation.

At the functional level, we performed pharmacological rescue experiments using CCT020312, a PERK pathway activator, to assess whether reactivation of PERK–eIF2α–ATF4 signaling could alleviate the effects of RUNX1 silencing. Compared with control HTSFs, RUNX1 silencing significantly impaired HTSF wound closure, whereas treatment with CCT020312 substantially alleviated this migration defect (Figure 5m and n). Transwell assays similarly revealed that RUNX1 silencing significantly reduced the number of migrated cells, whereas CCT020312 partially restored this effect (Figure 5o and p). WB analysis demonstrated that RUNX1 silencing decreased the levels of ATF4, BiP, p-PERK, and p-eIF2α and profibrotic proteins, whereas CCT020312 partially reversed these changes (Figure 5e–l). These data further support the role of ATF4 as an important downstream mediator of RUNX1 and suggest that reactivation of PERK-related ER stress signaling partially restores the profibrotic phenotype suppressed by RUNX1 silencing.

RUNX1 maintains ferroptosis resistance in HTSFs partly through ATF4

Because the preceding findings suggested that RUNX1 regulates the HTSF state through an ATF4-associated ER stress network, we next examined whether the RUNX1/ATF4 axis contributes to ferroptosis resistance. At the single-cell level, the ferroptosis-related score of Cluster 4 was relatively low (Figure 6a), suggesting that

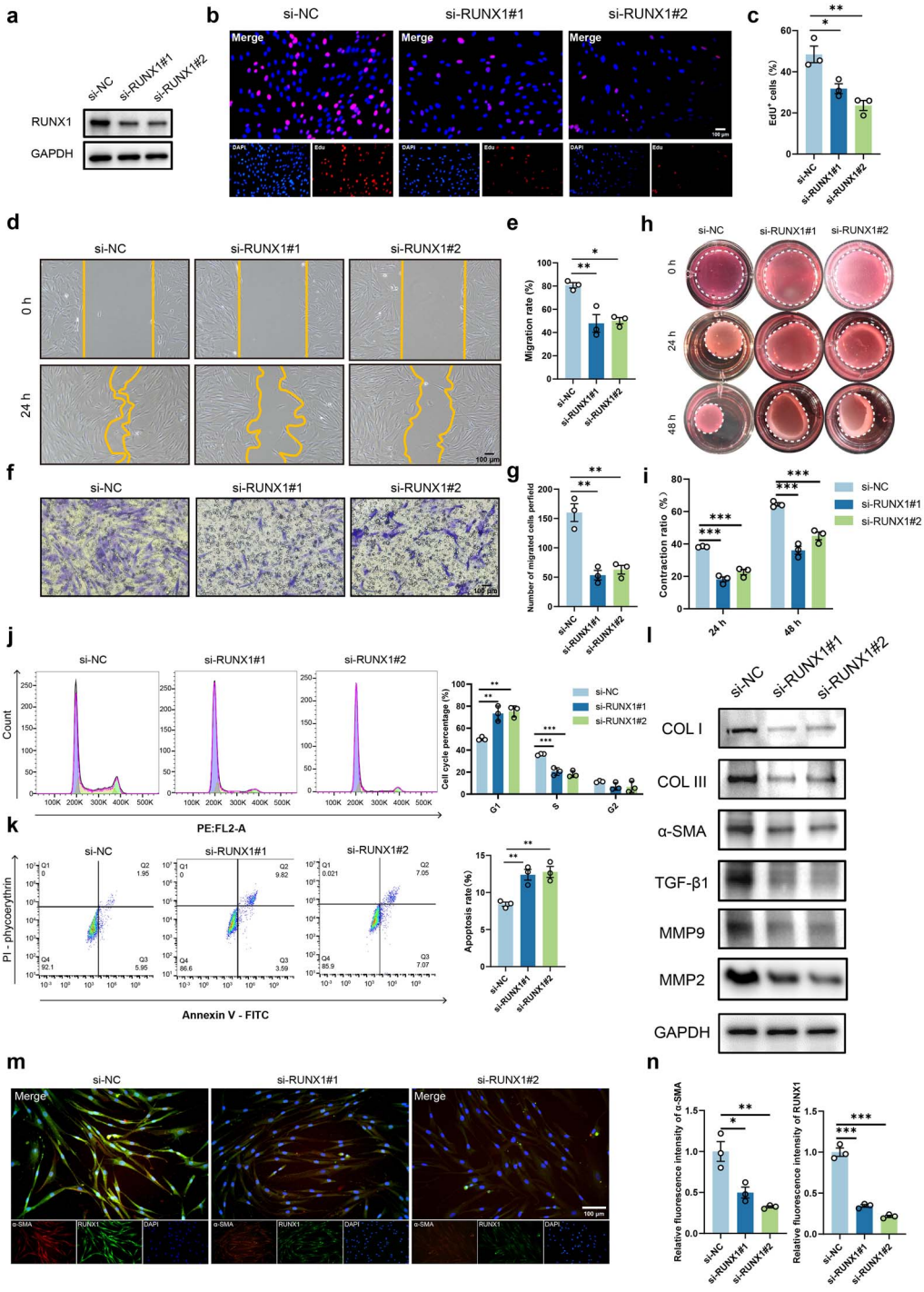


Figure 3 RUNX1 silencing suppresses the activation and profibrotic phenotype of HTSFs. (**a**) Western blot analysis of RUNX1 protein expression in HTSFs transfected with si-NC, si-RUNX1#1, and si-RUNX1#2. (**b**) EdU assay showing the proliferative capacity of HTSFs after RUNX1 silencing. Scale bar: 100 μm. (**c**) Quantification of the percentage of EdU-positive cells. (**d**) Wound-healing assay showing representative images at 0 and 24 h after RUNX1 silencing. Scale bar: 100 μm. (**e**) Quantification of the migration rate in the wound-healing assay. (**f**) Transwell assay showing representative images of HTSF migration after RUNX1 silencing. Scale bar: 100 μm. (**g**) Quantification of the number of migrated cells per field in the Transwell assay. (**h**) Time-course collagen gel contraction assay showing representative images of the same gels at 0, 24, and 48 h after RUNX1 silencing. (**i**) Quantification of the gel contraction ratios at 24 and 48 h relative to the corresponding initial gel area at 0 h. (**j**) Flow cytometric analysis and quantification of cell-cycle distribution in HTSFs after RUNX1 silencing. (**k**) Annexin V-FITC/PI flow cytometry and quantification of apoptosis in HTSFs after RUNX1 silencing. (**l**) Western blot analysis of COL I, COL III, α-SMA, TGF-β1, MMP2, and MMP9 protein expression in HTSFs after RUNX1 silencing. (**m**) Immunofluorescence staining showing RUNX1 and α-SMA expression in HTSFs under the indicated conditions. Scale bar: 100 μm. (**n**) Quantification of the relative fluorescence intensities of α-SMA and RUNX1, normalized to the si-NC group. Data are presented as mean $\pm$ SD; $n = 3$ biological replicates per group. Comparisons among three groups were performed using ordinary one-way ANOVA followed by Tukey's multiple-comparisons test. $^{*}P < 0.05$, $^{**}P < 0.01$, $^{***}P < 0.001$. *HTSF* hypertrophic scar fibroblast, *FITC* fluorescein isothiocyanate, *PI* propidium iodide, *α-SMA* alpha-smooth muscle actin, *SD* standard deviation

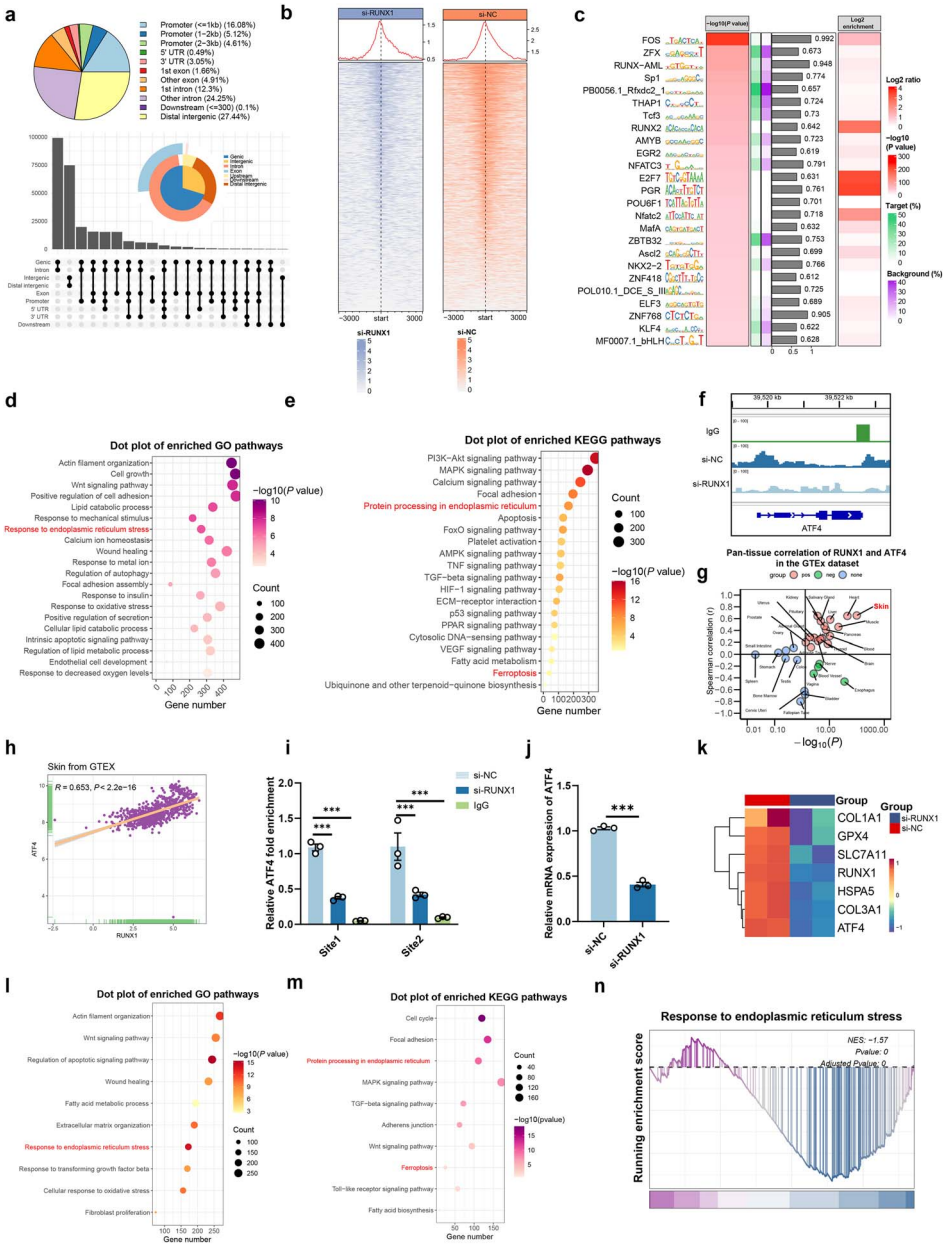


Figure 4 CUT&Tag combined with transcriptomic analysis identifies an ATF4-related ER stress and ferroptosis regulatory network downstream of RUNX1. (**a**) Genomic annotation of RUNX1 CUT&Tag peaks, showing their distribution across promoters, introns, exons, and distal intergenic regions. (**b**) CUT&Tag signal distribution around TSSs in si-NC and si-RUNX1 HTSFs. (**c**) Motif enrichment analysis of RUNX1-associated CUT&Tag peaks. (**d**) GO biological process enrichment analysis of genes associated with RUNX1 CUT&Tag peaks. (**e**) KEGG pathway enrichment analysis of genes associated with RUNX1 CUT&Tag peaks. (**f**) Genome browser tracks showing RUNX1 CUT&Tag signals at the ATF4 locus in the IgG control, si-NC, and si-RUNX1 groups. (**g**, **h**) Correlation analysis of RUNX1 and ATF4 expression in the GTEx database, including pan-tissue and skin-specific analyses. (**i**) CUT&Tag-qPCR analysis showing RUNX1 enrichment at two selected sites within the ATF4 promoter in the si-NC, si-RUNX1, and IgG control groups. (**j**) qPCR analysis of ATF4 mRNA expression after RUNX1 silencing. (**k**) Heatmap of selected differentially expressed genes in si-NC and si-RUNX1 HTSFs based on RNA-seq analysis. (**l**) GO biological process enrichment analysis of differentially expressed genes after RUNX1 silencing. (**m**) KEGG pathway enrichment analysis of differentially expressed genes after RUNX1 silencing. (**n**) GSEA showing downregulation of the response to endoplasmic reticulum stress gene set in the si-RUNX1 group. For (i) and (j), data are presented as mean ± SD; $n = 3$ biological replicates per group. Comparisons in (i) were performed using ordinary one-way ANOVA followed by Tukey's multiple-comparisons test for each site, and the comparison in (j) was performed using an unpaired two-tailed Student's *t*-test. $^{***}P < 0.001$. *CUT&Tag* cleavage under targets and tagmentation, *TSS* transcription start site, *HTSF* hypertrophic scar fibroblast, *ER* endoplasmic reticulum, *UTR* untranslated region, *ECM* extracellular matrix, *NES* normalized enrichment score, *SD* standard deviation

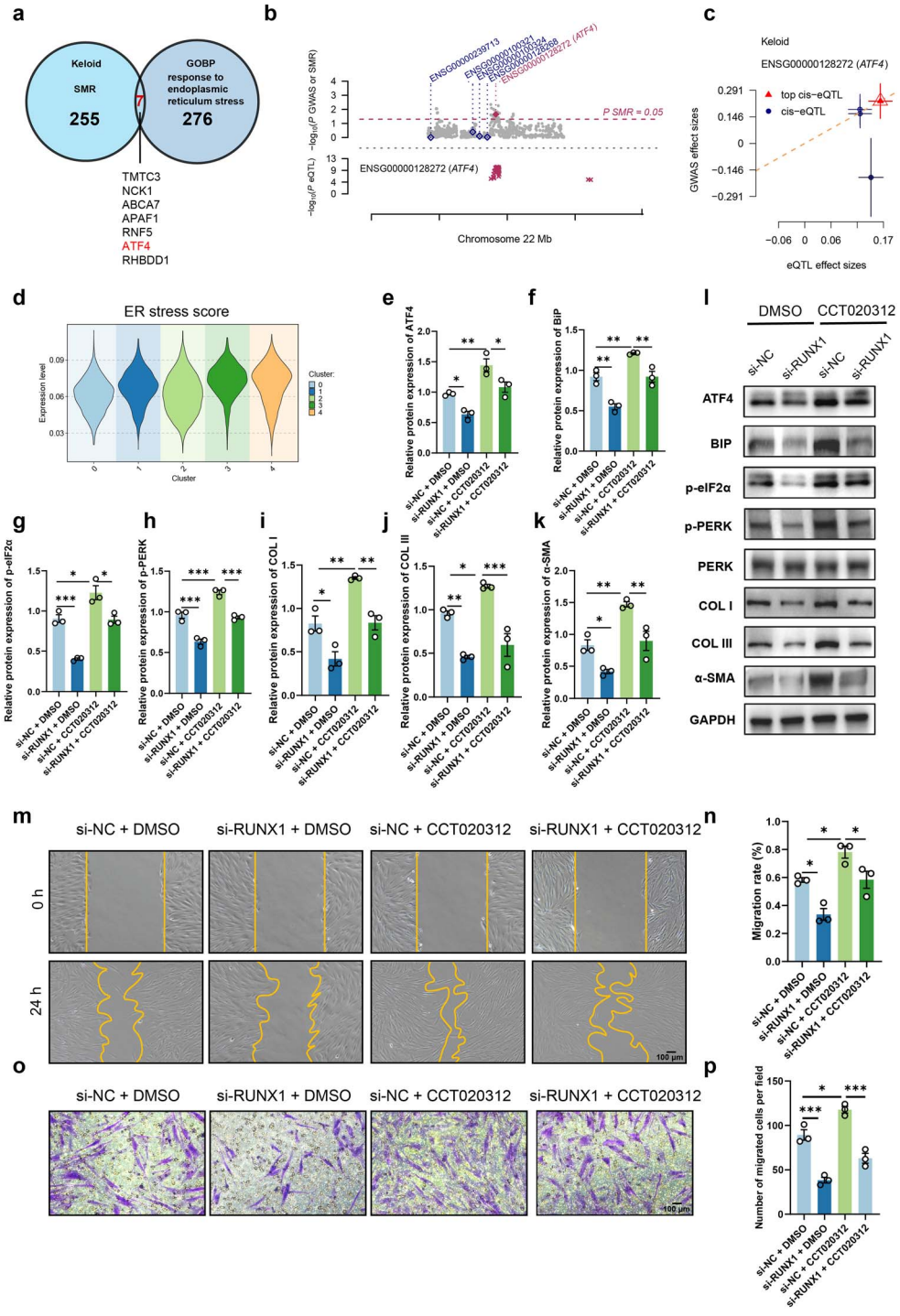


Figure 5 SMR analysis and pharmacological rescue experiments support the role of ATF4 as a downstream mediator of RUNX1. (**a**) SMR analysis integrating GTEx skin eQTL data with BioBank Japan keloid GWAS data, showing the associations of ER stress–related genes with keloid risk. ATF4 showed a nominal association. (**b**) Regional association plot at the ATF4 locus showing the distributions of the local eQTL and GWAS association signals. (**c**) Scatter plot comparing the *cis*-eQTL effects on ATF4 expression with the corresponding GWAS effects on keloid risk. (**d**) Comparison of ER stress scores across fibroblast subpopulations in single-cell transcriptomic analysis. (**e**–**l**) Western blot analysis and densitometric quantification of ATF4, BiP, p-eIF2α, p-PERK, PERK, COL I, COL III, and α-SMA protein expression in HTSFs under the indicated treatment conditions, including pharmacological activation of PERK signaling with CCT020312. (**m**, **n**) Wound-healing assay and quantification of HTSF migration under the indicated treatment conditions. Scale bar: 100 μm. (**o**, **p**) Transwell assay and quantification of HTSF migration under the indicated treatment conditions. Scale bar: 100 μm. For (e–k, n, p), data are presented as mean ± SD; $n = 3$ independent experiments per group. Statistical comparisons were performed using ordinary one-way ANOVA followed by Tukey's multiple-comparisons test. $^{*}P < 0.05$, $^{**}P < 0.01$, $^{***}P < 0.001$. *SMR* summary-data-based Mendelian randomization, *GTEx* Genotype-Tissue Expression, *eQTL* expression quantitative trait locus, *GWAS* genome-wide association study, *GOBP* Gene Ontology biological process, *ER* endoplasmic reticulum, *BiP* binding immunoglobulin protein, *eIF2α* eukaryotic translation initiation factor 2 alpha, *PERK* protein kinase RNA-like endoplasmic reticulum kinase, *HTSF* hypertrophic scar fibroblast, *DMSO* dimethyl sulfoxide, *α-SMA* alpha-smooth muscle actin, *SD* standard deviation

these POSTN+ fibroblasts may reside in a relatively ferroptosis-resistant state. A similar trend was observed for POSTN+ fibroblasts from the independent keloid single-cell dataset (Figure S12b). Together with the RUNX1-dependent changes in SLC7A11 and GPX4 expression and ferroptosis-related signaling identified by transcriptomic and RUNX1 CUT&Tag-associated pathway analyses, these findings prompted us to investigate whether RUNX1-high POSTN+ fibroblasts exhibit a ferroptosis resistance state associated with ATF4-related stress adaptation. The results of functional experiments revealed that treatment with ferrostatin-1 (Fer-1) significantly attenuated the increases in total ROS, lipid ROS, and intracellular Fe^{2+} levels induced by si-RUNX1 while also alleviating the reduction in cell viability (Figure S9a–f), indicating that the loss of RUNX1 expression sensitized HTSFs to ferroptosis-related injury. To directly assess GPX4-dependent ferroptosis susceptibility after RUNX1 knockdown, si-NC- and si-RUNX1-transfected HTSFs were treated with RAS-selective lethal 3 (RSL3), a GPX4-targeting ferroptosis inducer. Compared with si-NC cells, si-RUNX1 cells exposed to RSL3 exhibited a further decrease in cell viability and increased intracellular Fe^{2+} levels, indicating increased susceptibility to GPX4 inhibition-induced ferroptotic injury. GPX4 overexpression was confirmed by qPCR (Figure S10a). Compared with the si-RUNX1 + RSL3 group, GPX4 overexpression significantly increased cell viability (mean difference, 22.33; 95% CI, 13.75–30.92; Tukey-adjusted $P = 4.93 \times 10^{-5}$) and decreased intracellular Fe^{2+} levels (mean difference, −0.596; 95% CI, 0.320–0.871; Tukey-adjusted $P = 2.44 \times 10^{-4}$; Figure S10b and c), supporting a partial rescue effect.

We then performed rescue experiments in which ATF4 was overexpressed. JC-1 staining revealed that RUNX1 silencing reduced the mitochondrial membrane potential, whereas ATF4 overexpression partially improved this aberration (Figure 6b). Flow cytometric analysis revealed that RUNX1 silencing significantly increased total ROS and lipid ROS levels, whereas ATF4 overexpression significantly alleviated these changes (Figure 6c–f). CCK-8 assays revealed that the reduction in cell viability caused by RUNX1 knockdown was partially reversed by ATF4 overexpression (Figure 6g). Furthermore, si-RUNX1 significantly promoted intracellular Fe^{2+} and MDA accumulation while reducing GSH levels, and these changes were partially reversed by ATF4 overexpression (Figure 6h–j). In addition, ATF4 overexpression partially restored the reduced migratory capacity and the decreased expression of SLC7a11, GPX4, COL I, COL III, and α-SMA caused by RUNX1 silencing (Figure 6k–p). Together, these results indicate that RUNX1 loss increases ferroptosis susceptibility in HTSFs and that ATF4 is an important downstream mediator of this process.

To complement the ATF4 overexpression experiments, we examined the effects of single and combined RUNX1 and ATF4 silencing in HTSFs. Reverse transcription quantitative polymerase chain reaction (RT-qPCR) confirmed ATF4 knockdown in the si-ATF4 and combined groups (Figure S11a). ATF4 silencing recapitulated RUNX1 silencing, reducing COL1A1, ACTA2, SLC7A11, and GPX4 expression, decreasing cell viability, and increasing basal intracellular Fe^{2+} levels (Figure S11b–g). Combined silencing caused no further changes in these downstream readouts compared with RUNX1 silencing alone. This nonadditive pattern supports a downstream role for ATF4 in RUNX1-regulated fibroblast activation and ferroptosis-related cellular homeostasis.

POSTN+ fibroblasts contribute to angiogenesis-associated microenvironmental remodeling through RUNX1–MDK-dependent paracrine signaling

Because HTS lesions are often accompanied by persistent erythema and aberrant vascularization, we first examined endothelial cell abundance in a single-cell dataset and found that compared with those in NS, endothelial cells were significantly enriched in HTS (Figure 7a). Among the fibroblast subpopulations, the pathogenic POSTN+ cluster had the highest angiogenesis score (Figure 7b), suggesting a potential role in angiogenesis-associated microenvironmental remodeling. Similarly, in the independent keloid single-cell dataset, the angiogenesis score of the POSTN+ fibroblast subset was relatively elevated (Figure S12c). We then reanalyzed fibroblasts from the systemic sclerosis single-cell RNA-seq dataset and identified four fibroblast subclusters (Figure S13a). Among the fibroblast subclusters, Cluster 0 was enriched in both RUNX1 and POSTN and exhibited the highest angiogenesis-related score (Figure S13b and c). Together, the HTS, keloid, and systemic sclerosis datasets consistently associated POSTN+ fibroblasts with angiogenesis-related features, suggesting that this fibroblast phenotype may not be restricted to HTS. CellChat analysis revealed extensive fibroblast–endothelial communication in HTS, with a strong interaction number and strength (Figure 7c). Notably, midkine (MK) signaling was prominently enriched in this network, with fibroblasts acting as major signal senders toward endothelial cells (Figure 7d and e), and ligand–receptor analysis highlighted MDK-related interactions in this axis (Figure 7f). A similar fibroblast–endothelial communication pattern, including prominent MK signaling toward endothelial cells, was independently detected in the keloid dataset (Figure S12d–g), further supporting the relevance of this paracrine signaling pattern across pathological skin fibrosis. Consistent with these findings, MDK expression was preferentially enriched in the pathogenic POSTN+ fibroblast subset (Figure 7g).

We next investigated whether MDK might be transcriptionally regulated by RUNX1. CUT&Tag tracks revealed a RUNX1 binding signal at the MDK locus, which was reduced after RUNX1 silencing (Figure 7h). GTEx analysis showed a positive correlation between RUNX1 and MDK expression across tissues and in skin tissue specifically (Figure 7i and k). In addition, on the basis of motif prediction and CUT&Tag peak profiles, we selected two candidate RUNX1 binding regions within the MDK promoter for CUT&Tag–qPCR validation. Compared with those in the IgG control group, RUNX1 enrichment in the si-NC group at both Sites 1 and 2 was significantly greater, whereas the enrichment at both sites was significantly lower after RUNX1 was silenced (Figure 7l). qPCR further revealed that MDK mRNA expression decreased significantly after RUNX1 knockdown (Figure 7m). Similarly, RNA-seq analysis revealed reduced MDK expression in si-RUNX1-treated HTSFs compared with control HTSFs (Figure 7j). Together, these data support MDK as a downstream target associated with RUNX1-mediated proangiogenic signaling.

Functionally, conditioned medium from si-RUNX1-treated HTSFs significantly impaired HUVEC migration, proliferation, and

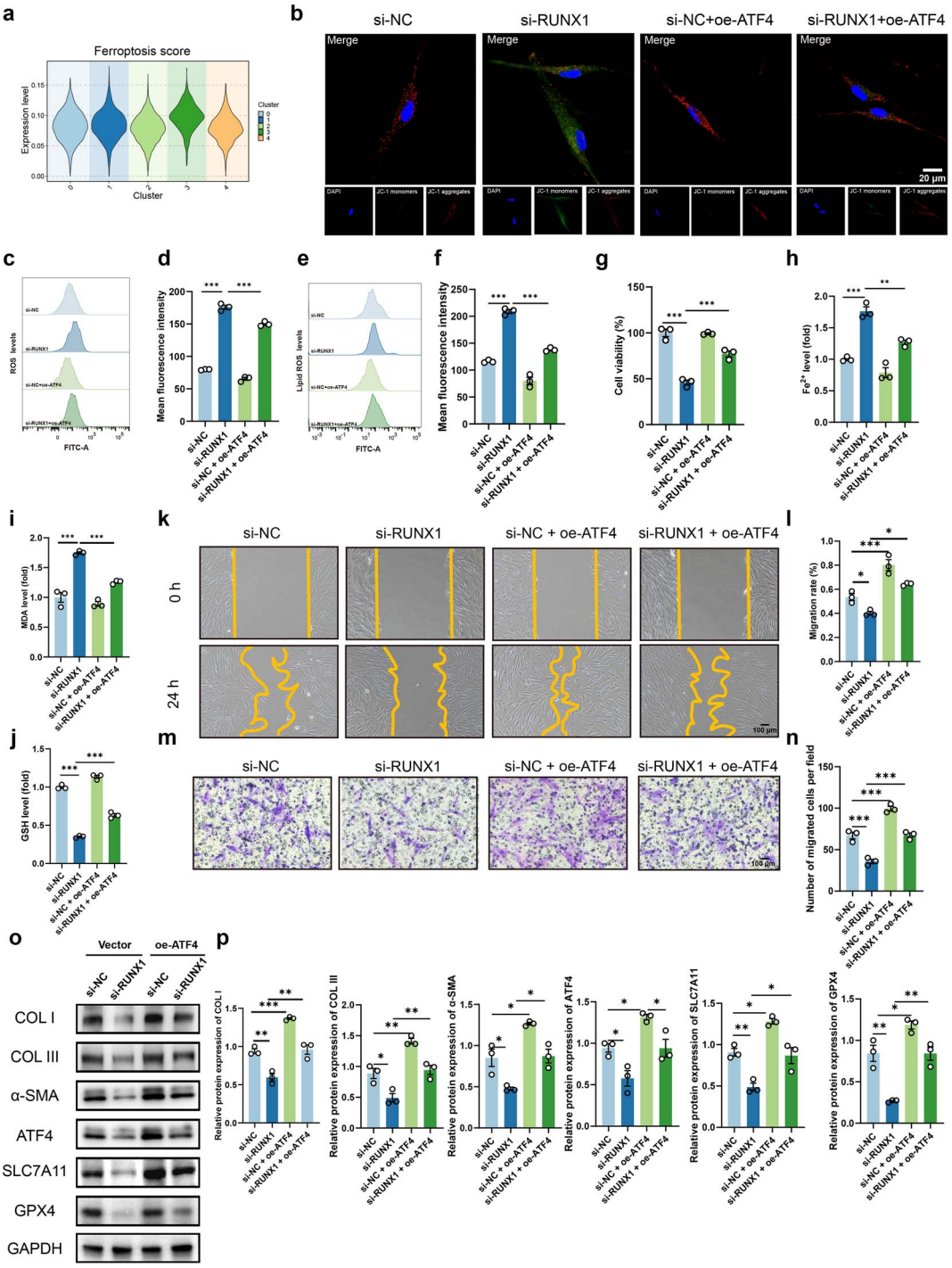


Figure 6 ATF4 overexpression partially reverses ferroptosis-related injury and the suppression of the profibrotic phenotype induced by RUNX1 silencing. (**a**) Comparison of ferroptosis-related signature scores across fibroblast subpopulations in single-cell transcriptomic analysis, showing a lower ferroptosis score in Cluster 4, the POSTN+ fibroblast subpopulation. (**b**) JC-1 fluorescence staining for assessment of mitochondrial membrane potential. Red fluorescence corresponds to JC-1 aggregates, whereas green fluorescence corresponds to JC-1 monomers. Scale bar: 20 μm. (**c**, **d**) Flow cytometric analysis and quantification of total ROS levels in HTSFs under the indicated treatment conditions. (**e**, **f**) Flow cytometric analysis and quantification of lipid ROS levels in HTSFs under the indicated treatment conditions. (**g**) CCK-8 assay evaluating cell viability in the indicated groups. (**h**–**j**) Measurement of intracellular Fe^{2+}, MDA, and GSH levels in the indicated groups. (**k**, **l**) Wound-healing assay and quantification of HTSF migration under the indicated conditions. Scale bar: 100 μm. (**m**, **n**) Transwell assay and quantification of HTSF migration under the indicated conditions. Scale bar: 100 μm. (**o**, **p**) Western blot analysis and densitometric quantification of ATF4, SLC7A11, GPX4, COL I, COL III, and α-SMA protein expression in the indicated groups. Data are presented as mean ± SD; $n = 3$ independent experiments per group. Comparisons among four groups were performed using ordinary one-way ANOVA followed by Tukey's multiple-comparisons test. $^{*}P < 0.05$, $^{**}P < 0.01$, $^{***}P < 0.001$. *HTSF* hypertrophic scar fibroblast, *ROS* reactive oxygen species, *MDA* malondialdehyde, *GSH* glutathione, *FITC* fluorescein isothiocyanate, *α-SMA*, alpha-smooth muscle actin, *si-NC*, negative-control small interfering RNA, *oe* overexpression, *SD* standard deviation

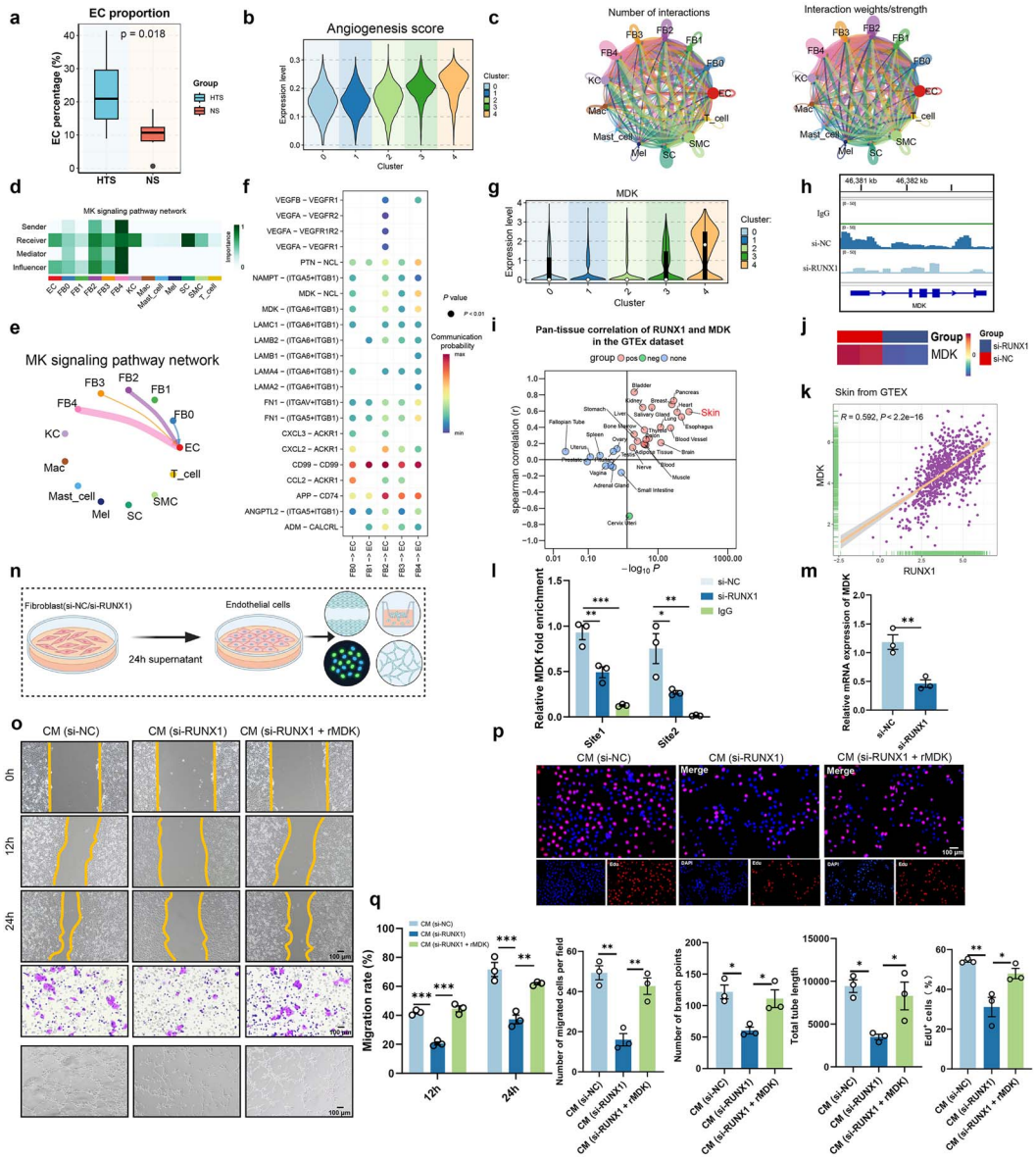


Figure 7 POSTN+ fibroblasts contribute to angiogenesis-associated microenvironmental remodeling through RUNX1–MDK-dependent paracrine signaling. (**a**) Comparison of endothelial cell proportions between HTS and NS in the single-cell dataset. (**b**) Angiogenesis scores across fibroblast subpopulations. (**c**) CellChat analysis showing the number and strength of intercellular interactions in HTS, highlighting fibroblast–endothelial communication. (**d**, **e**) MK signaling pathway network inferred by CellChat, showing fibroblasts as major signal senders toward endothelial cells. (**f**) Ligand–receptor interaction analysis in the fibroblast–endothelial communication network, highlighting MDK-related interactions. (**g**) Violin plot showing MDK expression across fibroblast subpopulations. (**h**) Genome browser tracks showing RUNX1 CUT&Tag signals at the MDK locus in the IgG control, si-NC, and si-RUNX1 groups. (**i**, **k**) Correlation analysis of RUNX1 and MDK expression in the GTEx database, including pan-tissue and skin-specific analyses. (**j**) Heatmap from RNA-seq analysis showing reduced MDK expression in si-RUNX1-treated HTSFs compared with the control group. (**l**) CUT&Tag-qPCR analysis showing RUNX1 enrichment at two selected sites within the MDK promoter in the si-NC, si-RUNX1, and IgG control groups. (**m**) qPCR analysis of MDK mRNA expression after RUNX1 silencing. (**n**) Schematic illustration of the conditioned-medium experiment using supernatants from si-NC- or si-RUNX1-treated fibroblasts, with or without recombinant human MDK supplementation, for HUVEC functional assays. (**o**) Wound-healing, Transwell migration, and tube formation assays showing HUVEC migratory and angiogenic capacities under the indicated conditioned-medium treatments. Scale bar: 100 μm. (**p**) EdU staining showing HUVEC proliferation under the indicated conditioned-medium treatments. Scale bar: 100 μm. (**q**) Quantification of migration rate, migrated cell number, EdU-positive cells, branch point number, and total tube length in HUVECs under the indicated conditions. Data are presented as mean ± SD; $n = 3$ biological replicates per group. For (a), an unpaired two-tailed Student's *t*-test was used. For (l), comparisons among three groups were performed separately for each site using ordinary one-way ANOVA followed by Tukey's multiple-comparisons test. For (m), the two-group comparison was performed using an unpaired two-tailed Student's *t*-test. For (q), comparisons among three groups were performed using ordinary one-way ANOVA followed by Tukey's multiple-comparisons test; migration rates were analyzed separately at each time point. Spearman correlation analysis was used in (i) and (k). $^{*}P < 0.05$, $^{**}P < 0.01$, $^{***}P < 0.001$. *HTS* hypertrophic scar, *NS* normal skin, *CUT&Tag* cleavage under targets and tagmentation, *IgG* immunoglobulin G, *GTEx*, Genotype-Tissue Expression, *HTSF* hypertrophic scar fibroblast, *HUVEC* human umbilical vein endothelial cell, *CM* conditioned medium, *SD* standard deviation

tube formation, whereas supplementation with recombinant human MDK partially reversed these defects (Figure 7n–q). These findings suggest that RUNX1-high POSTN+ fibroblasts contribute to angiogenesis-associated microenvironmental remodeling through MDK-dependent paracrine signaling.

In silico analyses prioritize BBR as a candidate compound with predicted potential to bind to POSTN

Given the importance of RUNX1 in pathogenic POSTN+ fibroblasts and the difficulty associated with directly targeting transcription factors, we next sought a more tractable downstream molecule for therapeutic intervention. CUT&Tag analysis revealed a clear RUNX1 binding signal at the POSTN locus, which was distinctly reduced after RUNX1 silencing (Figure 8a). Transcriptomic analysis revealed reduced POSTN expression in si-RUNX1-treated HTSFs compared with that in the control group (Figure 8b). Consistent with these findings, public transcriptomic datasets showed positive associations between RUNX1 and POSTN expression across SSc, keloid, and HTS cohorts (Figure 8c). In addition, on the basis of motif prediction and the CUT&Tag peak profiles, we selected two candidate RUNX1-binding regions within the POSTN promoter for CUT&Tag–qPCR validation. Compared with those in the IgG control group, RUNX1 enrichment in the si-NC group at both Sites 1 and 2 was significantly greater, whereas the enrichment at both sites was significantly lower following RUNX1 silencing (Figure 8e). qPCR confirmed that POSTN mRNA expression was significantly decreased after RUNX1 was silenced (Figure 8d). Together, these findings support POSTN as a downstream target associated with RUNX1 in pathogenic fibroblasts.

Virtual screening against POSTN was performed using a filtered TCMSP-derived compound library. Compounds with oral bioavailability (OB) $\geq$ 30%, drug likeness (DL) $\geq$ 0.18, and downloadable 3d mol2 structures were retained, resulting in 2102 candidate compounds, from which the top 20 were selected on the basis of predicted binding affinity. Among these candidates, BBR was computationally prioritized for subsequent investigation after considering its docking performance and previous literature supporting its regulatory effects on ER stress– and ferroptosis-related pathways, as well as its potential antifibrotic relevance (Figure 8f). Molecular docking suggested that BBR could be accommodated within a predicted POSTN binding pocket through interactions with multiple local residues (Figure 8g). During the molecular dynamics simulation, the equilibration parameters of the POSTN–BBR complex, including pressure, potential energy, density, and temperature, were monitored, and the results supported the overall stability of the system (Figure S14a–d). Further analyses of the RMSD, RMSF, and radius of gyration and hydrogen bond formation supported the stability of the POSTN–BBR complex (Figure 8h–k). Free energy landscape and principal component analyses revealed that the complex converged into a relatively restricted low-energy conformational state during the simulation (Figure 8l and m**)**. Structural analyses based on representative conformations illustrated the predicted interaction pose, local residue contacts, ligand conformational distribution, and electrostatic features of the putative POSTN interaction interface, supporting a stable and plausible predicted interaction mode between BBR and POSTN (Figure 8n–p). MM-GBSA analysis supported an energetically favorable predicted interaction between BBR and POSTN and revealed that POSTN residues contributed favorably to the computational estimate (Figure S15a and b).

BBR suppresses RUNX1/POSTN-associated ER stress adaptation, ferroptosis resistance, and profibrotic activation in HTSFs

We next examined the effects of BBR on HTSFs at the molecular level. CCK-8 assays revealed that BBR reduced HTSF viability in a dose-dependent manner, with an IC50 of 90.87 μM (Figure 9a). On the basis of these results, 50 μM BBR, a sub-IC50 concentration, was selected for subsequent mechanistic experiments because it resulted in a measurable reduction in cell viability without excessive cytotoxicity. RNA-seq revealed broad transcriptional changes after BBR treatment, as shown by the volcano plot and heatmap of differentially expressed genes (Figure 9b and c). Notably, RUNX1/POSTN axis–related and stress-adaptive genes, including RUNX1, POSTN, HSPA5, ATF4, GPX4, and SLC7a11, were downregulated in the BBR-treated group (Figure 9d). GO and KEGG analyses revealed enrichment of pathways related mainly to ER stress, intracellular iron ion homeostasis, ferroptosis, and protein processing in the ER (Figure 9e). GSEA confirmed the significant suppression of gene sets associated with the response to fibroblast growth factor, iron ion homeostasis, and the response to ER stress after BBR treatment (Figure 9f).

To assess whether these effects were linked to RUNX1, we performed rescue experiments in which RUNX1 was overexpressed. EdU staining revealed that BBR significantly inhibited HTSF proliferation, whereas RUNX1 overexpression partially reversed this effect (Figure 9g and i). Time-course collagen gel contraction assays similarly showed that BBR reduced matrix contractility, which was partially restored by RUNX1 overexpression (Figure S16a and b). JC-1 staining indicated that BBR reduced the mitochondrial membrane potential, whereas this change was alleviated by RUNX1 overexpression (Figure 9h). Furthermore, BBR increased the intracellular Fe^{2+} and MDA levels while decreasing the GSH content, and these changes were partially reversed by RUNX1 overexpression (Figure 9j–l), suggesting that BBR weakened the ferroptosis resistance maintained by RUNX1.

Consistently, WB revealed that BBR reduced the expression of POSTN, α-SMA, BiP, p-PERK, p-eIF2α, ATF4, GPX4, and SLC7a11, whereas RUNX1 overexpression restored the expression of these proteins to varying degrees (Figure 9m–v). To determine whether the downregulation of RUNX1 was associated with POSTN-dependent feedback, POSTN was silenced using two independent siRNAs. Both siRNAs efficiently reduced POSTN mRNA expression and also significantly decreased RUNX1 mRNA levels (Figure S17a and b), suggesting that POSTN may contribute to the maintenance of RUNX1 expression in HTSFs. Consistent with these findings, BBR treatment significantly reduced RUNX1 mRNA expression (Figure S17c). Together with our finding that RUNX1 directly transcriptionally activates POSTN, these results are consistent with a potential positive regulatory relationship between RUNX1 and POSTN. Disruption of this regulatory loop may partially contribute to the reduction in RUNX1 expression following BBR

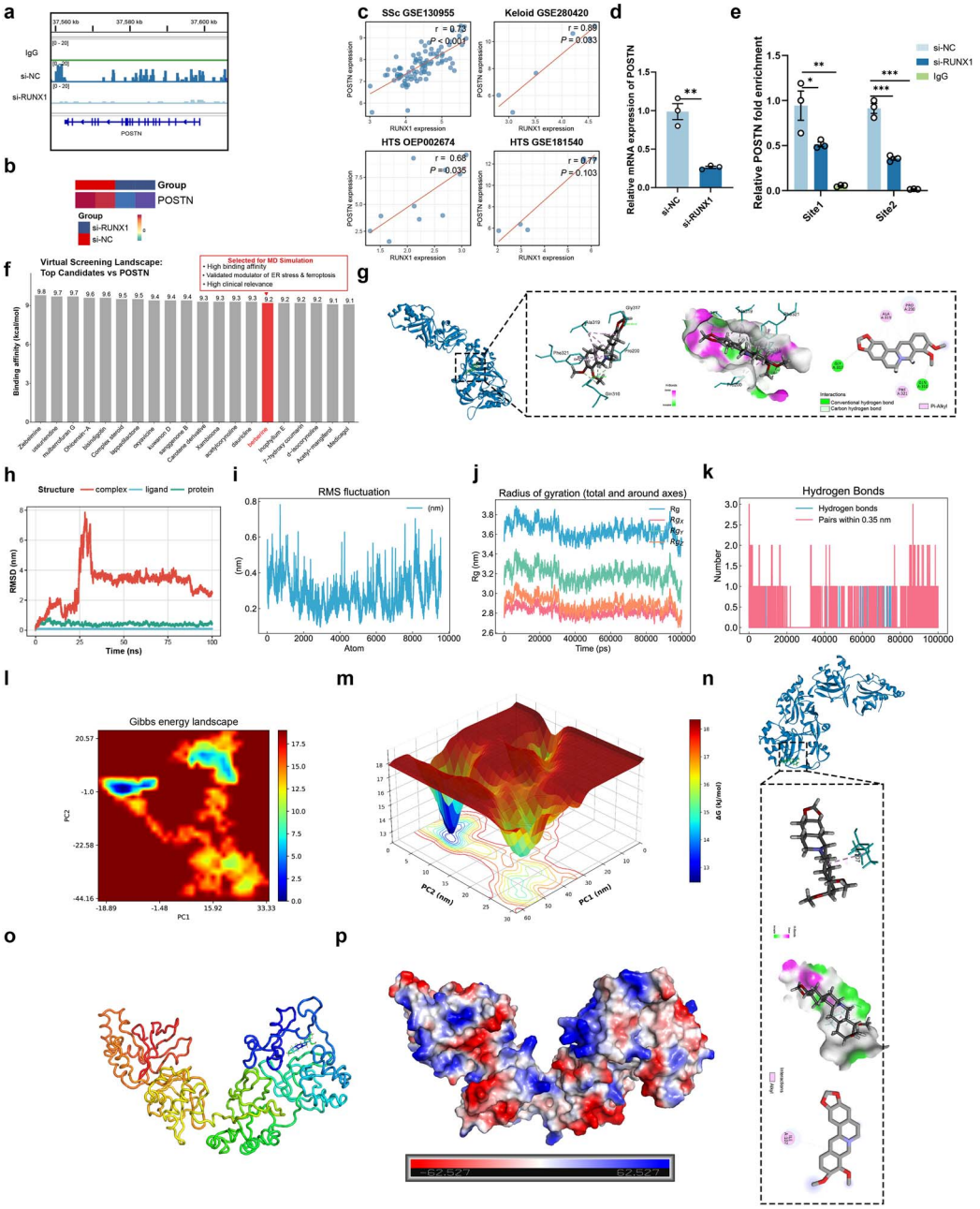


Figure 8 RUNX1-associated regulation of POSTN and *in silico* analyses prioritize BBR as a candidate compound predicted to bind to POSTN. (**a**) CUT&Tag tracks showing RUNX1 occupancy at the POSTN locus. (**b**) Heatmap from RNA-seq analysis showing reduced POSTN expression in si-RUNX1-treated HTSFs compared with control group. (**c**) Correlation analysis between RUNX1 and POSTN expression across public datasets from SSc, keloid, and HTS. (**d**) qPCR analysis of POSTN mRNA expression after RUNX1 silencing. (**e**) CUT&Tag-qPCR analysis showing RUNX1 enrichment at the selected candidate region within the POSTN promoter in si-NC, si-RUNX1, and IgG control groups. (**f**) Virtual screening results showing the top 20 candidate compounds ranked by predicted binding affinity against POSTN from a TCMSP-derived compound library. (**g**) Molecular docking model of BBR with POSTN. (**h**) RMSD curves of the POSTN–BBR complex and related components during molecular dynamics simulation. (**i**) RMSF analysis of the POSTN–BBR complex. (**j**) Radius of gyration analysis of the complex. (**k**) Time-dependent changes in hydrogen bond number between POSTN and BBR. (**l**, **m**) Free energy landscape and principal component analyses of the POSTN–BBR complex. (**n**) Structural interaction analysis showing a representative predicted binding pose of BBR within the predicted POSTN pocket together with local residue contacts and interaction pattern. (**o**) Conformational distribution analysis of the POSTN–BBR complex during molecular dynamics simulation. (**p**) Surface electrostatic mapping of the POSTN binding interface. Data are presented as mean ± SD; $n = 3$ biological replicates per group for (d) and (e). For (d), the two-group comparison was performed using an unpaired two-tailed Student's *t*-test. For (e), comparisons among three groups were performed separately for each site using ordinary one-way ANOVA followed by Tukey's multiple-comparisons test. Spearman's rank correlation was used in (c). $^{*}P < 0.05$, $^{**}P < 0.01$, $^{***}P < 0.001$. *BBR* berberine, *CUT&Tag* cleavage under targets and tagmentation, *HTSF* hypertrophic scar fibroblast, *SSc* systemic sclerosis, *HTS* hypertrophic scar, *IgG* immunoglobulin G, *TCMSP* Traditional Chinese Medicine Systems Pharmacology, *RMSD* root mean square deviation, *RMSF* root mean square fluctuation, *SD* standard deviation

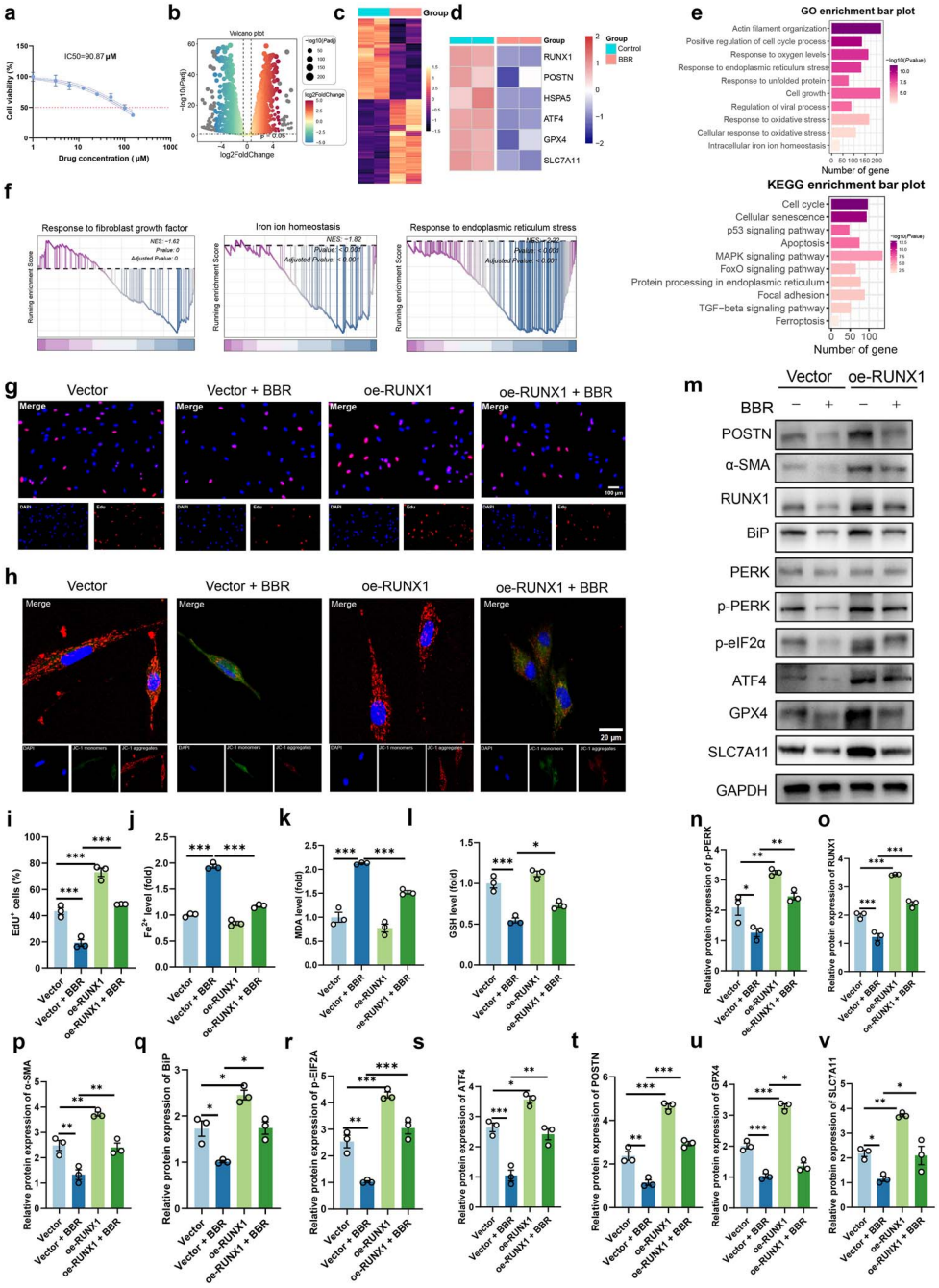


Figure 9 BBR suppresses RUNX1/POSTN-associated ER stress adaptation, ferroptosis resistance, and profibrotic activation in HTSFs. (**a**) CCK-8 assay showing the effect of BBR on HTSF viability and the calculated IC50 value. (**b**) Volcano plot of differentially expressed genes between the control and BBR-treated groups. (**c**) Heatmap of differentially expressed genes between the control and BBR-treated groups. (**d**) Heatmap showing the expression changes of RUNX1, POSTN, HSPA5, ATF4, GPX4, and SLC7A11 after BBR treatment. (**e**) GO and KEGG functional enrichment analyses of differentially expressed genes in BBR-treated HTSFs. (**f**) GSEA showing altered enrichment of gene sets related to response to fibroblast growth factor, iron ion homeostasis, and response to endoplasmic reticulum stress after BBR treatment. (**g**) EdU staining showing the proliferative capacity of HTSFs under the indicated treatment conditions. Scale bar: 100 μm. (**h**) JC-1 fluorescence staining for assessment of mitochondrial membrane potential in HTSFs under the indicated treatment conditions. Red fluorescence represents JC-1 aggregates, whereas green fluorescence represents JC-1 monomers. Scale bar: 20 μm. (**i**) Quantification of the percentage of EdU-positive cells. (**j**–**l**) Measurement of intracellular Fe^{2+}, MDA, and GSH levels, respectively, in the indicated groups. (**m**) Western blot analysis of POSTN, α-SMA, RUNX1, BiP, PERK, p-PERK, p-eIF2α, ATF4, GPX4, and SLC7A11 protein expression in HTSFs under the indicated conditions. (**n**–**v**) Densitometric quantification of the protein expression shown in (m). Data are presented as mean ± SD; $n = 3$ biological replicates per group. For four-group comparisons, ordinary one-way ANOVA followed by Tukey's multiple-comparisons test was used. $^{*}P < 0.05$, $^{**}P < 0.01$, $^{***}P < 0.001$. *BBR* berberine, *ER* endoplasmic reticulum, *HTSF* hypertrophic scar fibroblast, *MDA* malondialdehyde *GSH* glutathione, *BiP* binding immunoglobulin protein, *α-SMA* alpha-smooth muscle actin, *SD* standard deviation

treatment. Taken together, these findings indicate that BBR suppresses RUNX1/POSTN-associated ER stress adaptation, ferroptosis resistance, and profibrotic activation in HTSFs, which is accompanied by suppression of the RUNX1 axis.

RUNX1 silencing attenuates skin fibrosis *in vivo*, whereas BBR exerts antifibrotic effects

To validate the *in vivo* contribution of RUNX1 to skin fibrosis, we first established a bleomycin-induced dermal fibrosis model combined with AAV9-mediated RUNX1 silencing (Figure 10a). Because this model recapitulates key features of systemic sclerosis-like dermal fibrosis, it was used to evaluate whether RUNX1 is required for fibrotic progression *in vivo*. Compared with AAV9-ctrl mice, AAV9-shRUNX1 mice had markedly reductions in dermal thickness and Masson-positive collagen area (Figure 10b and c). Histological analysis further revealed that RUNX1 silencing alleviated dermal thickening, collagen accumulation, and disorganized collagen fiber deposition, as demonstrated by H&E staining, Masson's trichrome staining, and Sirius Red staining under both bright-field and polarized light microscopy (Figure 10d–g). Immunohistochemistry confirmed the efficient reduction in RUNX1 expression in AAV9-shRUNX1-treated fibrotic skin (Figure 10h and k). Consistent with these findings, immunofluorescence staining revealed decreased POSTN and α-SMA expression and reduced ATF4 and GPX4 signaling after RUNX1 was silenced (Figure 10i, j, and l–o). WB analysis confirmed that AAV9-shRUNX1 reduced the protein levels of COL III, COL I, α-SMA, POSTN, RUNX1, ATF4, and GPX4 in bleomycin-induced fibrotic skin tissues (Figure 10p–w). These findings indicate that local AAV9-mediated RUNX1 silencing attenuates bleomycin-induced skin fibrosis and is associated with reduced matrix remodeling and ATF4-associated stress-adaptive features *in vivo*.

We next examined whether RUNX1 also contributes to scar formation in a mouse scar model (Figure 11a). Compared with AAV9-ctrl, AAV9-shRUNX1 significantly reduced the scar elevation index, Masson-positive collagen area, and area with positive staining for RUNX1 (Figure 11b–d). H&E and Masson's trichrome staining revealed that RUNX1 silencing decreased scar thickness and collagen deposition, whereas immunohistochemical staining for RUNX1 confirmed reduced RUNX1 expression in scar tissues (Figure 11e–g). Immunofluorescence staining demonstrated that AAV9-shRUNX1 decreased GPX4 and ATF4 expression, as well as POSTN and α-SMA expression, in scar tissues, with corresponding quantitative analyses confirming these reductions (Figure 11h and i and Figure S18a–d). At the molecular level, WB revealed that RUNX1 silencing reduced the expression of fibrotic markers, including COL III, COL I, α-SMA, and POSTN, together with RUNX1, ATF4, and GPX4-related signals (Figure 11j–q). These results further support that local AAV9-mediated RUNX1 silencing reduces scar formation and attenuates fibrotic tissue remodeling *in vivo*.

Finally, we assessed the therapeutic effect of BBR in a rabbit ear scar model (Figure 11r). Compared with vehicle treatment, treatment with BBR reduced scar thickness, collagen deposition, and α-SMA expression, with a more pronounced inhibitory effect detected at higher concentrations (Figure 11s–u). Quantitative analysis confirmed that BBR significantly decreased the Masson-positive area and tissue thickness in rabbit ear scar tissue (Figure 11v and w). Together, the results of these complementary animal experiments show that local RUNX1 suppression attenuates skin fibrosis and scar-associated tissue remodeling *in vivo*, whereas the results of a rabbit ear model support the antiscar efficacy of BBR, as it results in reduced fibroproliferative remodeling.

Discussion

Skin fibrosis diseases, including HTS, KS, and SSc, are characterized by persistent fibroblast activation and progressive matrix remodeling [40, 41]. Recent studies have further suggested that fibrotic progression may be sustained by the selective expansion of pathogenic fibroblast states rather than the generalized activation of all fibroblasts [6, 42]. Our study aimed to define the fibroblast state most relevant to skin fibrosis progression and the mechanism underlying its persistence.

In this study, POSTN+ fibroblasts were expanded in skin fibrosis and exhibited features consistent with those of activated myofibroblasts. POSTN-expressing fibroblast populations have also been implicated in pulmonary and cardiac fibrosis [9, 17]. However, fibroblast states are shaped by organ-specific microenvironments and exhibit species-dependent heterogeneity, and findings from noncutaneous fibrosis models therefore cannot be directly extrapolated to skin fibrosis. Our analyses revealed relative enrichment of POSTN+ fibroblasts in both HTS and KS. These findings support the notion that POSTN+ fibroblasts are a disease-associated fibroblast state in various skin fibrosis diseases and suggest that they may contribute to the persistent fibroblast activation and matrix remodeling common to HTS and KS. Moreover, the distinct clinical and pathological manifestations of HTS and KS are likely shaped by broader disease-specific factors, including differences in mechanical tension, immune and inflammatory responses, vascular conditions, and local cell–cell interactions, in addition to potential differences in the abundance and tissue distribution of POSTN+ fibroblasts [1, 3].

Having established the relevance of this fibroblast state to skin fibrosis, we next investigated the upstream mechanisms that sustain it. RUNX1 emerged as a candidate upstream regulator because of its preferential enrichment within POSTN+ fibroblasts. Previous studies have implicated RUNX1 in fibrotic remodeling in the heart, liver, lung, and systemic sclerosis [11, 13, 14, 16]. However, its role in regulating a POSTN+ fibroblast state across skin fibrosis diseases, including HTS, KS, and SSc, has not been systematically defined. Within the POSTN+ fibroblast populations identified in both HTS and KS, RUNX1 expression was elevated, while concordant RUNX1–POSTN associations were also detected in the SSc-related datasets. Together, these findings support a shared RUNX1-high POSTN+ disease-associated fibroblast state across skin fibrosis diseases. Functionally, RUNX1 silencing attenuated fibroblast activation and profibrotic phenotypes, whereas integrated multiomic analyses and experimental validation supported the direct transcriptional regulation of POSTN by RUNX1. Thus, our findings extend those of previous RUNX1-related fibrosis studies by identifying RUNX1 as an upstream regulator of a disease-associated POSTN+ fibroblast state in skin fibrosis rather than merely confirming its association with general fibroblast activation.

Fibrotic skin lesions exist in a high-stress microenvironment marked by abnormal mechanical tension, sustained extracellular matrix biosynthetic demand, oxidative stress, and chronic

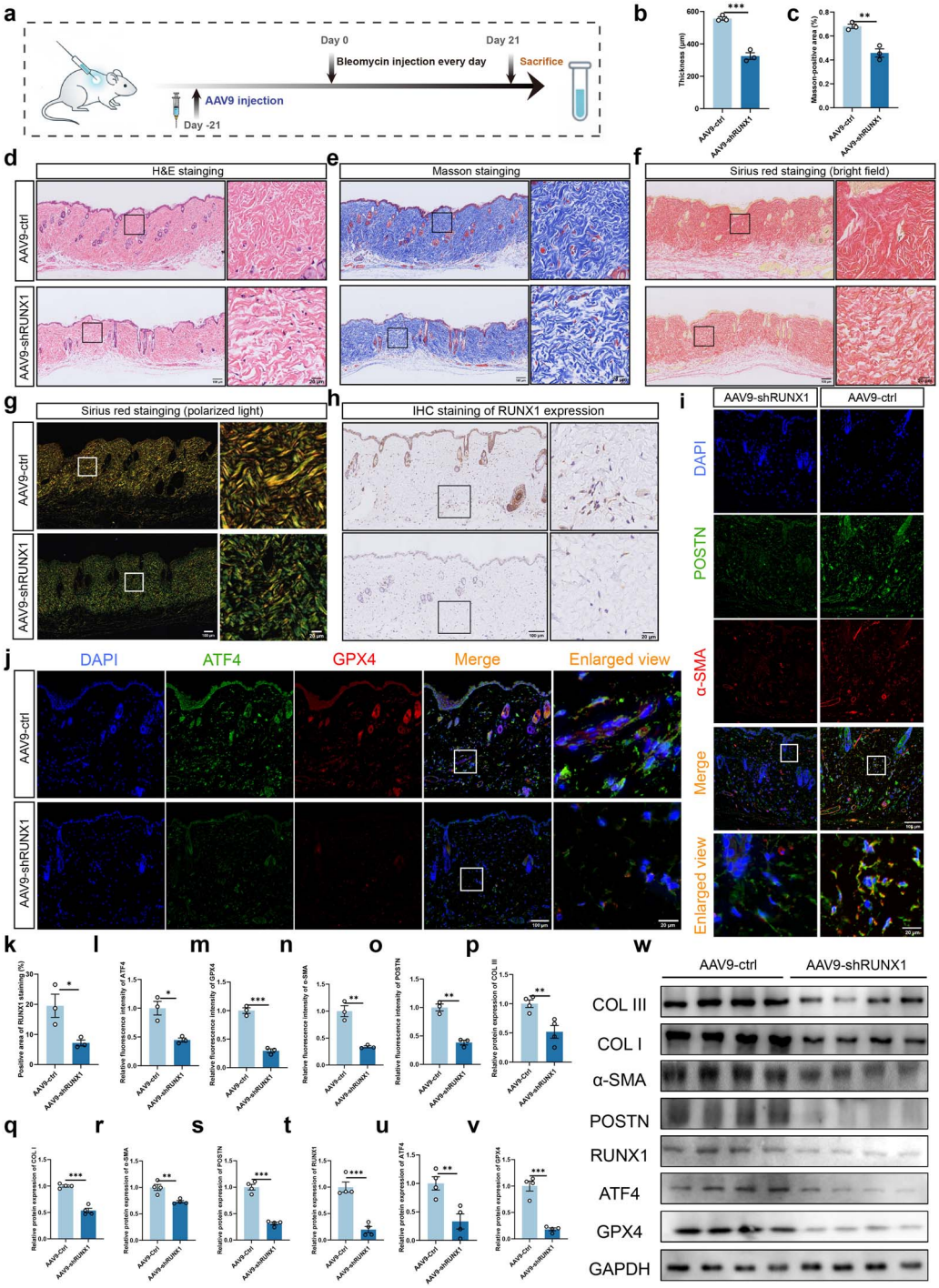


Figure 10 RUNX1 silencing attenuates bleomycin-induced skin fibrosis *in vivo*. (**a**) Schematic diagram of the bleomycin-induced skin fibrosis model and AAV9 intervention timeline. AAV9-shRUNX1 or AAV9-ctrl was administered before daily bleomycin challenge. (**b**) Quantification of skin thickness in the AAV9-ctrl and AAV9-shRUNX1 groups. $n = 3$ mice per group. (**c**) Quantification of Masson-positive collagen area, normalized to the total tissue area within each field. $n = 3$ mice per group. (**d**) H&E staining showing histological changes in bleomycin-induced fibrotic skin tissues. Scale bar: 100 μm; 20 μm. (**e**) Masson's trichrome staining showing collagen deposition in the indicated groups. Scale bar: 100 μm; 20 μm. (**f**) Sirius Red staining under bright-field microscopy showing collagen fiber distribution. Scale bar: 100 μm; 20 μm. (**g**) Sirius Red staining under polarized light showing collagen fiber organization in the indicated groups. Scale bar: 100 μm; 20 μm. (**h**) Immunohistochemical staining of RUNX1 expression in mouse skin tissues. Scale bar: 100 μm; 20 μm. (**i**) Immunofluorescence staining showing POSTN and α-SMA expression in the indicated groups. Scale bar: 100 μm; 20 μm. (**j**) Immunofluorescence staining showing ATF4 and GPX4 expression in the indicated groups. Scale bar: 100 μm; 20 μm. (**k**) Quantification of RUNX1-positive staining area, normalized to the total tissue area within each field. $n = 3$ mice per group. (**l**–**o**) Quantification of the relative fluorescence intensity of ATF4, GPX4, α-SMA, and POSTN. $n = 3$ mice per group. (**p**–**v**) Quantification of the relative protein expression levels of COL III, COL I, α-SMA, POSTN, RUNX1, ATF4, and GPX4. $n = 4$ mice per group. (**w**) Western blot analysis of COL III, COL I, α-SMA, POSTN, RUNX1, ATF4, and GPX4 protein expression in mouse skin tissues. $n = 4$ mice per group. Data are presented as mean ± SD. Two-group comparisons were performed using an unpaired two-tailed Student's *t*-test. $^{*}P < 0.05$, $^{**}P < 0.01$, $^{***}P < 0.001$. *AAV9* adeno-associated virus serotype 9, *H&E* hematoxylin and eosin, *IHC* immunohistochemistry, *α-SMA* alpha-smooth muscle actin, *SD* standard deviation

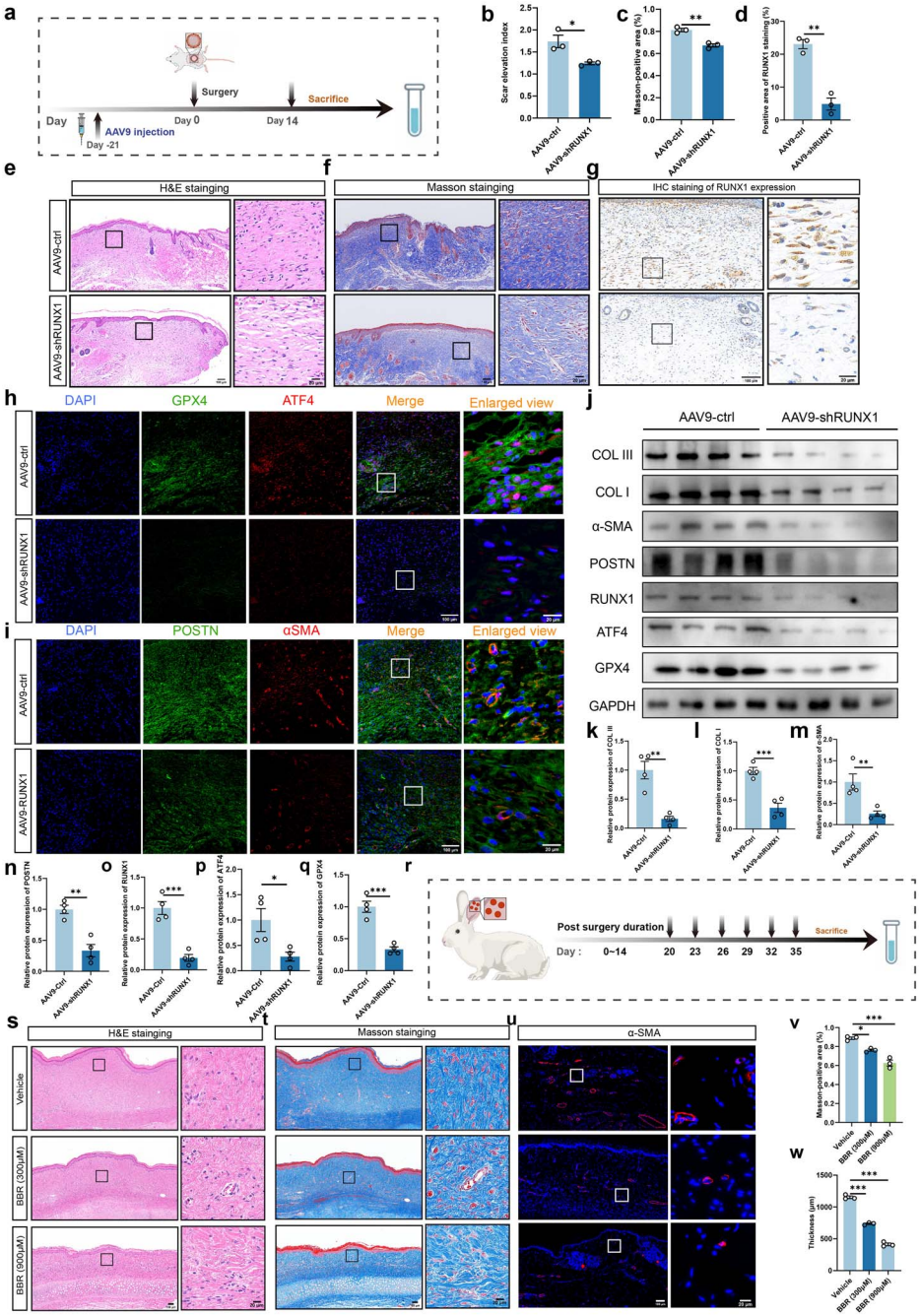


Figure 11 RUNX1 silencing suppresses scar formation in mice, whereas BBR attenuates fibroproliferative remodeling in a rabbit ear scar model. (**a**) Schematic diagram of the mouse scar model and AAV9 intervention timeline. (**b**–**d**) Quantification of scar elevation index, Masson-positive area, and RUNX1-positive staining area in the AAV9-ctrl and AAV9-shRUNX1 groups. Masson-positive collagen area and RUNX1-positive staining area were normalized to the total tissue area within each field. $n = 3$ mice per group. (**e**) H&E staining showing scar morphology and tissue thickness in the indicated groups. Scale bar: 100 μm; 20 μm. (**f**) Masson's trichrome staining showing collagen deposition in mouse scar tissues. Scale bar: 100 μm; 20 μm. (**g**) Immunohistochemical staining of RUNX1 expression in mouse scar tissues. Scale bar: 100 μm; 20 μm. (**h**) Immunofluorescence staining showing GPX4 and ATF4 expression in scar tissues. Scale bar: 100 μm; 20 μm. (**i**) Immunofluorescence staining showing POSTN and α-SMA expression in scar tissues. Scale bar: 100 μm; 20 μm. (**j**) Western blot analysis of COL III, COL I, α-SMA, POSTN, RUNX1, ATF4, and GPX4 protein expression in mouse scar tissues. $n = 4$ mice per group. (**k**–**q**) Quantification of the relative protein expression levels of COL III, COL I, α-SMA, POSTN, RUNX1, ATF4, and GPX4. $n = 4$ mice per group. (**r**) Schematic diagram of the rabbit ear scar model and BBR treatment schedule. (**s**) H&E staining showing scar thickness in the Vehicle, BBR (300 μM), and BBR (900 μM) groups. Scale bar: 100 μm; 20 μm. (**t**) Masson's trichrome staining showing collagen deposition in rabbit ear scar tissues. Scale bar: 100 μm. (**u**) Immunofluorescence staining of α-SMA in rabbit ear scar tissues after BBR treatment. Scale bar: 100 μm; 20 μm. (**v**, **w**) Quantification of Masson-positive area and tissue thickness in the rabbit ear scar model. $n = 3$ biological replicates per group. Data are presented as mean ± SD. Two-group comparisons were performed using an unpaired two-tailed Student's *t*-test. Comparisons among three groups were performed using ordinary one-way ANOVA followed by Tukey's multiple-comparisons test. $^{*}P < 0.05$, $^{**}P < 0.01$, $^{***}P < 0.001$. *AAV9* adeno-associated virus serotype 9, *BBR* berberine; *H&E* hematoxylin and eosin, *IHC* immunohistochemistry, *α-SMA* alpha-smooth muscle actin, *SD* standard deviation

inflammatory stimulation [20, 43, 44]. Consistent with these observations, ER stress–related features were enriched in the pathogenic POSTN+ fibroblast state in skin fibrosis. Previous work in noncutaneous fibrosis has already established that ER stress is not simply an accompanying event but one that can actively promote fibroblast activation and fibrotic remodeling. In idiopathic pulmonary fibrosis, ER stress directly facilitates lung fibroblast-to-myofibroblast differentiation, whereas in liver fibrosis, inhibition of IRE1α suppresses myofibroblast activation and reduces fibrosis [18, 45]. Similar observations have also been reported in cutaneous fibrotic diseases: systemic sclerosis fibroblasts display ultrastructural and transcriptional evidence of ER stress, including increased BiP and ATF4 expression, and keloid studies support a profibrotic role of the PERK–eIF2α–ATF4 branch [46, 47]. A key advance of the present study is that RUNX1 is upstream of the PERK–eIF2α–ATF4 axis in pathogenic POSTN+ fibroblasts. SMR analysis provided genetic prioritization of ATF4 as a fibrosis-related candidate mediator, whereas CUT&Tag, transcriptomic analysis, and functional rescue experiments supported its downstream regulation by RUNX1. Pharmacological rescue experiments strengthened this interpretation. These findings suggest that activated ATF4-associated ER stress signaling in pathogenic POSTN+ fibroblasts is not merely a reflection of biosynthetic burden but may instead provide an adaptive advantage that helps sustain fibroblast persistence during skin fibrotic remodeling.

Building on the stress-adaptive features described above, a critical question is how pathogenic POSTN+ fibroblasts persist under sustained oxidative and metabolic stress. Our study further suggests that RUNX1 promotes ferroptosis resistance in pathogenic POSTN+ fibroblasts through an ATF4–SLC7A11/GPX4-dependent axis. Ferroptosis, an iron-dependent form of lipid peroxidation–driven cell death, has been increasingly implicated as a mechanism limiting the accumulation of pathogenic mesenchymal cells [48]. In scleroderma skin fibroblasts, erastin-induced ferroptosis is suppressed, and GPX4 upregulation confers ferroptosis resistance, supporting the idea that antiferroptotic buffering contributes to fibroblast persistence [22]. Ferroptosis-related alterations have been linked to keloid biology, and pharmacologic modulation of ferroptosis can influence keloid fibroblast behavior [49]. This interpretation is supported by our previous work, in which bruceine D alleviated skin fibrosis by targeting PIM1 and inducing ferroptosis in myofibroblasts, thereby highlighting ferroptotic elimination as a critical mechanism limiting pathogenic fibroblast accumulation [4]. In this context, the present findings suggest that pathogenic POSTN+ fibroblasts in skin fibrosis exhibit a ferroptosis-resistant phenotype. These observations suggest that RUNX1 promotes ferroptosis resistance in pathogenic POSTN+ fibroblasts through an ATF4–SLC7A11/GPX4-dependent mechanism, thereby helping these cells evade ferroptotic clearance and persist in fibrotic lesions. Taken together, these findings indicate that RUNX1 supports the persistence of pathogenic POSTN+ fibroblasts not only by promoting their activation but also by protecting them from ferroptotic elimination.

In addition to fibroblast-intrinsic regulation, the present study further explored the interaction between RUNX1-high POSTN+ fibroblasts and endothelial cells. This focus is relevant to skin fibrosis because fibrotic skin lesions exhibit not only excessive matrix deposition but also vascular abnormalities, particularly in the context of systemic sclerosis, and aberrant angiogenic signaling in pathological scarring [50, 51]. In line with this, single-cell analysis revealed an expansion of endothelial cells across skin fibrotic diseases, supporting the notion that vascular remodeling is an integral component of the fibrotic niche. In this context, the RUNX1-high POSTN+ fibroblast state showed angiogenesis-associated features and preferential crosstalk with endothelial cells, at least in part through MDK-dependent paracrine signaling. Given the established proangiogenic and profibrotic activities of MDK, as well as its reported involvement in endothelial-to-mesenchymal transition [52–54], our findings suggest that RUNX1 may link POSTN+ fibroblast activation to vascular remodeling by transcriptionally activating MDK. Together, these results support a model in which a RUNX1-high POSTN+ fibroblast state may function not only as a matrix-associated fibroblast state but also as a niche organizer that helps shape the vascular microenvironment in skin fibrosis.

Virtual screening and structural analyses computationally prioritized BBR as a candidate compound predicted to bind to POSTN that is relevant to the RUNX1-high POSTN+ fibroblast state. *In vitro* mechanistic experiments revealed that BBR suppressed RUNX1/POSTN-associated profibrotic and stress-adaptive features, including the expression of ATF4-associated ER stress molecules and ferroptosis resistance markers, and these effects were partially reversed by RUNX1 overexpression. BBR also reduced scar thickness, collagen deposition, and α-SMA expression in the rabbit ear hypertrophic scar model, supporting its antiscar efficacy *in vivo*. This interpretation is consistent with the findings of previous studies showing that BBR suppresses ER stress and promotes ferroptosis. In the context of liver fibrosis, BBR has been reported to attenuate fibrosis progression in association with the suppression of ER stress, whereas other studies have suggested that BBR can also alleviate fibrosis by promoting the ferroptotic death of hepatic stellate cells [55]. Similarly, BBR has been shown to reduce fibrosis-related changes and attenuate ER stress during cardiac remodeling [56]. Together, these observations support the therapeutic value of BBR in skin fibrosis and further suggest that the RUNX1-high POSTN+ fibroblast state may represent a candidate therapeutic vulnerability rather than merely a marker of fibrosis-associated matrix production.

This study has several limitations. Although our data support a functional link between the RUNX1-high POSTN+ fibroblast state and skin fibrosis, we did not directly ablate or selectively inhibit POSTN+ fibroblasts *in vivo*, and local AAV9-mediated RUNX1 silencing was not fibroblast specific. Therefore, the causal contribution of POSTN+ fibroblasts and the fibroblast-intrinsic role of RUNX1 in fibrosis progression require further validation using cell state-specific or fibroblast-specific targeting strategies. The current work focused mainly on fibroblasts and their interaction with endothelial cells, whereas other components of the fibrotic niche, including immune cells, neural elements, and persistent mechanical stress, may also interact with the RUNX1 axis in skin fibrosis and thus warrant further investigation.

Conclusions

In conclusion, our study identifies RUNX1 as an upstream driver of a pathogenic POSTN+ fibroblast state in skin fibrosis. RUNX1 was consistently upregulated across HTS, KS, and SSc samples and was associated with fibrotic remodeling, supporting its

potential value as a biomarker of skin fibrosis. Mechanistically, RUNX1 directly transcriptionally activates ATF4, POSTN, and MDK, thereby coupling stress adaptation and ferroptosis resistance to maintenance of the activated POSTN+ fibroblast phenotype and angiogenesis-associated microenvironmental remodeling. In addition, virtual screening and structural analyses computationally prioritized BBR as a candidate compound predicted to bind to POSTN. Together with *in vitro* mechanistic validation and rabbit ear scar model efficacy data, these findings support BBR as a potential therapeutic candidate for skin fibrosis.

Acknowledgements

We thank the Analysis & Testing Laboratory for Life Sciences and Medicine of the Fourth Military Medical University for technical support.

Author contributions

Binyu Song (Conceptualization [lead], Data curation [equal], Investigation [equal], Writing—original draft [lead]), Yuhan Zhu (Conceptualization [equal], Investigation [lead], Methodology [equal]), Xiang Wang (Formal analysis [equal], Investigation [equal], Validation [equal]), Yige Han (Data curation [equal], Validation [equal], Visualization [equal]), Junying Song (Formal analysis [equal], Methodology [equal]), Kai Wang (Methodology [equal], Supervision [equal]), Tong Wang (Data curation [equal], Validation [equal]), Yixuan Peng (Formal analysis [equal], Visualization [equal]), Xiaozi Liu (Data curation [equal], Investigation [equal]), Zhiwei Cui (Formal analysis [equal], Validation [equal]), Guo Peng (Investigation [equal], Resources [equal]), Yajuan Song (Investigation [equal], Resources [equal]), Yi Shi (Investigation [equal], Resources [equal]), Zhou Yu (Conceptualization [equal], Resources [equal], Supervision [equal], Writing—review & editing [equal]), and Baoqiang Song (Funding acquisition [lead], Resources [lead], Supervision [lead], Writing—review & editing [lead])

Supplementary material

Supplementary material is available at *Burns & Trauma* online.

Conflicts of interest

The authors declare that they have no conflict of interest.

Funding

This work was financially supported by the National Natural Science Foundation of China (Grant Numbers 82372530, 82072182, and 82673296) and Innovative Medical Research Promotion Project of Xijing Hospital (XJZT24LZ14).

Data availability

The data that support the findings of this research can be obtained from the corresponding author upon reasonable request.

Ethics approval and consent to participate

This study was conducted in accordance with the Declaration of Helsinki and was approved by the ethics committee of the Fourth Military Medical University (approval no. 20250121).

References

1. Li DJ, Berry CE, Wan DC, Longaker MT. Clinical, mechanistic, and therapeutic landscape of cutaneous fibrosis. *Sci Transl Med* 2024;16:eadn7871. https://doi.org/10.1126/scitranslmed.adn7871.
2. Allanore Y, Simms R, Distler O, Trojanowska M, Pope J, Denton CP, *et al.* Systemic sclerosis. *Nat Rev Dis Primers* 2015;1:15002. https://doi.org/10.1038/nrdp.2015.2.
3. Talbott HE, Mascharak S, Griffin M, Wan DC, Longaker MT. Wound healing, fibroblast heterogeneity, and fibrosis. *Cell Stem Cell* 2022;29:1161–80. https://doi.org/10.1016/j.stem.2022.07.006.
4. Wang J, Song Y, Tan X, Wang T, Shi Y, Xu X, *et al.* Targeting PIM1 by Bruceine D attenuates skin fibrosis via myofibroblast ferroptosis. *Redox Biol* 2025;82:103619. https://doi.org/10.1016/j.redox.2025.103619.
5. Griffin MF, HE DJ-P, Mascharak S, Borrelli MR, Longaker MT. Understanding the impact of fibroblast heterogeneity on skin fibrosis. *Dis Model Mech* 2020;13:dmm044164. https://doi.org/10.1242/dmm.044164.
6. Deng CC, Hu YF, Zhu DH, Cheng Q, Gu JJ, Feng QL, *et al.* Single-cell RNA-seq reveals fibroblast heterogeneity and increased mesenchymal fibroblasts in human fibrotic skin diseases. *Nat Commun* 2021;12:3709. https://doi.org/10.1038/s41467-021-24110-y.
7. Zhang X, Zhang Y, Liu Y. Fibroblast activation and heterogeneity in fibrotic disease. *Nat Rev Nephrol* 2025;21:613–32. https://doi.org/10.1038/s41581-025-00969-8.
8. Ruiz-Villalba A, Pardo-Saganta A. Emerging concepts and novel mechanisms in organ fibrosis. *npj Regener Med* 2025;10:57. https://doi.org/10.1038/s41536-025-00446-7.
9. Xu L, Li T, Cao Y, He Y, Shao Z, Liu S, *et al.* PIEZO1 mediates periostin+ myofibroblast activation and pulmonary fibrosis in mice. *J Clin Invest* 2025;135:e184158. https://doi.org/10.1172/JCI184158.
10. Hong YK, Hwang DY, Yang CC, Cheng SM, Chen PC, Aala WJ, *et al.* Profibrotic subsets of SPP1(+) macrophages and POSTN(+) fibroblasts contribute to fibrotic scarring in acne keloidalis. *J Invest Dermatol* 2024;144:e10. https://doi.org/10.1016/j.jid.2023.12.014.
11. Dubey S, Dubey PK, Umeshappa CS, Ghebre YT, Krishnamurthy P. Inhibition of RUNX1 blocks the differentiation of lung fibroblasts to myofibroblasts. *J Cell Physiol* 2022;237:2169–82. https://doi.org/10.1002/jcp.30684.
12. O'Hare M, Amarnani D, Whitmore HAB, An M, Marino C, Ramos L, *et al.* Targeting runt-related transcription factor 1 prevents pulmonary fibrosis and reduces expression of severe acute respiratory syndrome coronavirus 2 host mediators. *Am J Pathol* 2021;191:1193–208. https://doi.org/10.1016/j.ajpath.2021.04.006.

13. Riddell A, McBride M, Braun T, Nicklin SA, Cameron E, Loughrey CM, *et al.* RUNX1: an emerging therapeutic target for cardiovascular disease. *Cardiovasc Res* 2020;116:1410–23. https://doi.org/10.1093/cvr/cvaa034.
14. Guo Z, Liu X, Zhao S, Sun F, Ren W, Ma M. RUNX1 promotes liver fibrosis progression through regulating TGF-beta signalling. *Int J Exp Pathol* 2023;104:188–98. https://doi.org/10.1111/iep.12474.
15. Zhou T, Luo M, Cai W, Zhou S, Feng D, Xu C, *et al.* Runt-related transcription factor 1 (RUNX1) promotes TGF-beta-induced renal tubular epithelial-to-mesenchymal transition (EMT) and renal fibrosis through the PI3K subunit p110delta. *EBioMedicine* 2018;31:217–25. https://doi.org/10.1016/j.ebiom.2018.04.023.
16. Parvizi R, Gong Z, Jarnagin HC, Toledo DM, Abel TR, Popovich D, *et al.* RUNX1 is expressed in a subpopulation of dermal fibroblasts and is associated with disease severity of systemic sclerosis. *Ann Rheum Dis* 2026;85:507–18. https://doi.org/10.1016/j.ard.2025.10.033.
17. Akins KA, Arkatkar A, Flinn MA, Sandor N, Purdy AL, Brusacoram AL, *et al.* Runx1 in Postn-expressing fibroblasts but not cardiomyocytes exacerbates adverse cardiac remodeling post-myocardial infarction. *JACC Basic Transl Sci* 2026;11:101455. https://doi.org/10.1016/j.jacbts.2025.101455.
18. Heindryckx F, Binet F, Ponticos M, Rombouts K, Lau J, Kreuger J, *et al.* Endoplasmic reticulum stress enhances fibrosis through IRE1alpha-mediated degradation of miR-150 and XBP-1 splicing. *EMBO Mol Med* 2016;8:729–44. https://doi.org/10.15252/emmm.201505925.
19. Chen X, Zhang J, Guo L, Wu C, Zhou J, Xu M, *et al.* Decoding organ fibrosis: mechanistic insights and emerging therapeutic strategies. *Signal Transduct Target Ther* 2026;11:82. https://doi.org/10.1038/s41392-025-02532-0.
20. Kropski JA, Blackwell TS. Endoplasmic reticulum stress in the pathogenesis of fibrotic disease. *J Clin Invest* 2018;128:64–73. https://doi.org/10.1172/JCI93560.
21. Han S, Lee M, Shin Y, Giovanni R, Chakrabarty RP, Herrerias MM, *et al.* Mitochondrial integrated stress response controls lung epithelial cell fate. *Nature* 2023;620:890–7. https://doi.org/10.1038/s41586-023-06423-8.
22. Zhang F, Xiao Y, Huang Z, Wang Y, Wan W, Zou H, *et al.* Upregulation of GPX4 drives ferroptosis resistance in scleroderma skin fibroblasts. *Free Radic Biol Med* 2024;221:23–30. https://doi.org/10.1016/j.freeradbiomed.2024.05.013.
23. Dixon SJ, Lemberg KM, Lamprecht MR, Skouta R, Zaitsev EM, Gleason CE, *et al.* Ferroptosis: an iron-dependent form of non-apoptotic cell death. *Cell* 2012;149:1060–72. https://doi.org/10.1016/j.cell.2012.03.042.
24. Friedmann Angeli JP, Schneider M, Proneth B, Tyurina YY, Tyurin VA, Hammond VJ, *et al.* Inactivation of the ferroptosis regulator Gpx4 triggers acute renal failure in mice. *Nat Cell Biol* 2014;16:1180–91. https://doi.org/10.1038/ncb3064.
25. Chen Y, Wang S, Mao C, Lu Q, Zhu X, Fan D, *et al.* 5-ALA photodynamic metabolite-powered zero-waste ferroptosis amplifier for enhanced hypertrophic scar therapy. *Nat Commun* 2025;16:8321. https://doi.org/10.1038/s41467-025-63438-7.
26. Ryan DG, Yang M, Prag HA, Blanco GR, Nikitopoulou E, Segarra-Mondejar M, *et al.* Disruption of the TCA cycle reveals an ATF4-dependent integration of redox and amino acid metabolism. *elife* 2021;10:e72593. https://doi.org/10.7554/eLife.72593.
27. Harding HP, Zhang Y, Zeng H, Novoa I, Lu PD, Calfon M, *et al.* An integrated stress response regulates amino acid metabolism and resistance to oxidative stress. *Mol Cell* 2003;11:619–33. https://doi.org/10.1016/s1097-2765(03)00105-9.
28. Cowan MJB, Davidson S, Coles M, Buckley CD. The role of fibroblasts across inflammation and immunity. *Annu Rev Pathol* 2026;21:423–45. https://doi.org/10.1146/annurev-pathmechdis-080624-105114.
29. Jarnagin HC, Parvizi R, Gong Z, Gedert R, Xing X, Tsoi LAC, *et al.* Multimodal analyses of early, untreated systemic sclerosis skin identify a proinflammatory vascular niche of macrophage-fibroblast signaling. *JCI Insight* 2026;11:e198954. https://doi.org/10.1172/jci.insight.198954.
30. Chen Y, Yin W, Liu Z, Lu G, Zhang X, Yang J, *et al.* Exosomes derived from fibroblasts enhance skin wound angiogenesis by regulating HIF-1alpha/VEGF/VEGFR pathway. Burns. *Trauma* 2025;13:tkae071. https://doi.org/10.1093/burnst/tkae071.
31. Stuart T, Butler A, Hoffman P, Hafemeister C, Papalexi E, Mauck WM 3rd, *et al.* Comprehensive integration of single-cell data. *Cell* 2019;177:e21. https://doi.org/10.1016/j.cell.2019.05.031.
32. Korsunsky I, Millard N, Fan J, Slowikowski K, Zhang F, Wei K, *et al.* Fast, sensitive and accurate integration of single-cell data with Harmony. *Nat Methods* 2019;16:1289–96. https://doi.org/10.1038/s41592-019-0619-0.
33. Jin S, Guerrero-Juarez CF, Zhang L, Chang I, Ramos R, Kuan CH, *et al.* Inference and analysis of cell-cell communication using CellChat. *Nat Commun* 2021;12:1088. https://doi.org/10.1038/s41467-021-21246-9.
34. Qiu X, Mao Q, Tang Y, Wang L, Chawla R, Pliner HA, *et al.* Reversed graph embedding resolves complex single-cell trajectories. *Nat Methods* 2017;14:979–82. https://doi.org/10.1038/nmeth.4402.
35. Zhu Z, Zhang F, Hu H, Bakshi A, Robinson MR, Powell JE, *et al.* Integration of summary data from GWAS and eQTL studies predicts complex trait gene targets. *Nat Genet* 2016;48:481–7. https://doi.org/10.1038/ng.3538.
36. Avouac J. Mouse model of experimental dermal fibrosis: the bleomycin-induced dermal fibrosis. *Methods Mol Biol* 2014;1142:91–8. https://doi.org/10.1007/978-1-4939-0404-4_11.
37. Blyszczuk P, Kozlova A, Guo Z, Kania G, Distler O. Experimental mouse model of bleomycin-induced skin fibrosis. *Curr Protoc Immunol* 2019;126:e88. https://doi.org/10.1002/cpim.88.
38. Griffin MF, Borrelli MR, Garcia JT, Januszyk M, King M, Lerbs T, *et al.* JUN promotes hypertrophic skin scarring via CD36 in preclinical in vitro and in vivo models. *Sci Transl Med* 2021;13:eabb3312. https://doi.org/10.1126/scitranslmed.abb3312.
39. Song B, Zhang W, Guo S, Han Y, Zhang Y, Ma F, *et al.* Adenovirus-mediated METH1 gene expression inhibits hypertrophic scarring in a rabbit ear model. *Wound Repair Regen* 2009;17:559–68. https://doi.org/10.1111/j.1524-475X.2009.00514.x.
40. Jeschke MG, Wood FM, Middelkoop E, Bayat A, Teot L, Ogawa R, *et al.* Scars. *Nat Rev Dis Primers* 2023;9:64. https://doi.org/10.1038/s41572-023-00474-x.
41. Gabrielli A, Avvedimento EV, Krieg T. Scleroderma. *N Engl J Med* 2009;360:1989–2003. https://doi.org/10.1056/NEJMra0806188.

42. Tabib T, Huang M, Morse N, Papazoglou A, Behera R, Jia M, *et al.* Myofibroblast transcriptome indicates SFRP2(hi) fibroblast progenitors in systemic sclerosis skin. *Nat Commun* 2021;12:4384. https://doi.org/10.1038/s41467-021-24607-6.
43. He J, Cheng X, Fang B, Shan S, Li Q. Mechanical stiffness promotes skin fibrosis via Piezo1-Wnt2/Wnt11-CCL24 positive feedback loop. *Cell Death Dis* 2024;15:84. https://doi.org/10.1038/s41419-024-06466-3.
44. Doridot L, Jeljeli M, Chene C, Batteux F. Implication of oxidative stress in the pathogenesis of systemic sclerosis via inflammation, autoimmunity and fibrosis. *Redox Biol* 2019;25:101122. https://doi.org/10.1016/j.redox.2019.101122.
45. Baek HA, Kim DS, Park HS, Jang KY, Kang MJ, Lee DG, *et al.* Involvement of endoplasmic reticulum stress in myofibroblastic differentiation of lung fibroblasts. *Am J Respir Cell Mol Biol* 2012;46:731–9. https://doi.org/10.1165/rcmb.2011-0121OC.
46. Lenna S, Farina AG, Martyanov V, Christmann RB, Wood TA, Farber HW, *et al.* Increased expression of endoplasmic reticulum stress and unfolded protein response genes in peripheral blood mononuclear cells from patients with limited cutaneous systemic sclerosis and pulmonary arterial hypertension. *Arthritis Rheum* 2013;65:1357–66. https://doi.org/10.1002/art.37891.
47. Kim S, Lee SE, Yi S, Jun S, Yi YS, Nagar H, *et al.* Tauroursodeoxycholic acid decreases keloid formation by reducing endoplasmic reticulum stress as implicated in the pathogenesis of keloid. *Int J Mol Sci* 2021;22:10765. https://doi.org/10.3390/ijms221910765.
48. Lai W, Wang B, Huang R, Zhang C, Fu P, Ma L. Ferroptosis in organ fibrosis: from mechanisms to therapeutic medicines. *J Transl Int Med* 2024;12:22–34. https://doi.org/10.2478/jtim-2023-0137.
49. Wang X, Yang Y, Zhou X, Yu S, Luo X, Lu L, *et al.* IFNgamma regulates ferroptosis in KFs by inhibiting the expression of SPOCD1 through DNMT3A. *Cell Death Discov* 2025;11:9. https://doi.org/10.1038/s41420-024-02257-z.
50. Volkmann ER, Andreasson K, Smith V. Systemic sclerosis. *Lancet* 2023;401:304–18. https://doi.org/10.1016/S0140-6736(22)01692-0.
51. Kumar AS, Kamalasanan K. Drug delivery to optimize angiogenesis imbalance in keloid: a review. *J Control Release* 2021;329:1066–76. https://doi.org/10.1016/j.jconrel.2020.10.035.
52. Filippou PS, Karagiannis GS, Constantinidou A. Midkine (MDK) growth factor: a key player in cancer progression and a promising therapeutic target. *Oncogene* 2020;39:2040–54. https://doi.org/10.1038/s41388-019-1124-8.
53. Weckbach LT, Groesser L, Borgolte J, Pagel JI, Pogoda F, Schymeinsky J, *et al.* Midkine acts as proangiogenic cytokine in hypoxia-induced angiogenesis. *Am J Physiol Heart Circ Physiol* 2012;303:H429–38. https://doi.org/10.1152/ajpheart.00934.2011.
54. Xu C, Chen J, Liang L, Chen S, Niu X, Sang R, *et al.* Midkine promotes renal fibrosis by stabilizing C/EBPbeta to facilitate endothelial-mesenchymal transition. *Commun Biol* 2024;7:544. https://doi.org/10.1038/s42003-024-06154-0.
55. Yi J, Wu S, Tan S, Qin Y, Wang X, Jiang J, *et al.* Berberine alleviates liver fibrosis through inducing ferrous redox to activate ROS-mediated hepatic stellate cells ferroptosis. *Cell Death Discov* 2021;7:374. https://doi.org/10.1038/s41420-021-00768-7.
56. Liao Y, Chen K, Dong X, Li W, Li G, Huang G, *et al.* Berberine inhibits cardiac remodeling of heart failure after myocardial infarction by reducing myocardial cell apoptosis in rats. *Exp Ther Med* 2018;16:2499–505. https://doi.org/10.3892/etm.2018.6438.

© The Author(s) 2026. Published by Oxford University Press. This is an Open Access article distributed under the terms of the Creative Commons Attribution-NonCommercial License (https://creativecommons.org/licenses/by-nc/4.0/), which permits non-commercial re-use, distribution, and reproduction in any medium, provided the original work is properly cited. For commercial re-use, please contact reprints@oup.com for reprints and translation rights for reprints. All other permissions can be obtained through our RightsLink service via the Permissions link on the article page on our site—for further information please contact journals.permissions@oup.com.
Burns & Trauma, 2026, 14, tkag063
https://doi.org/10.1093/burnst/tkag063
Research Article